Received 1 August 2024; revised 31 October 2024, 13 December 2024, and 21 February 2025; accepted 22 February 2025.
Date of publication 11 March 2025; date of current version 11 April 2025.
This article was recommended by Executive Editor Sanjiv Singh.

Digital Object Identifier 10.1109/TFR.2025.3547309

SailMAV: Water-Surface Locomotion and Biodiversity Monitoring

ANDRÉ FARINHA[1,2,3], LUCA ROMANELLO[1,2,4,5] (Graduate Student Member, IEEE), RAPHAEL ZUFFEREY[6] (Member, IEEE), JENNA LAWSON[1,7], SOPHIE FRANZISKA ARMANINI[4,8], AND MIRKO KOVAC[1,2,5]

[1]Aerial Robotics Laboratory, Imperial College London, SW7 2AZ London, U.K.
[2]Laboratory of Sustainability Robotics, EMPA, 8600 Dübendorf, Switzerland
[3]Robotic Design and Interaction Group, CSIRO, Pullenvale, QLD 4069, Australia
[4]eAviation Group, TUM, 80333 Munich, Germany
[5]Laboratory of Sustainability Robotics, EPFL, 1015 Lausanne, Switzerland
[6]AURA Lab, MIT, Cambridge, MA 02139 USA
[7]UK Centre for Ecology and Hydrology (UKCEH), LA1 4AP Lancaster, U.K.
[8]Department of Aeronautics, Imperial College London, SW7 2AZ London, U.K.

CORRESPONDING AUTHOR: LUCA ROMANELLO (luca.romanello@epfl.ch)

This article has supplementary downloadable material available at https://doi.org/10.1109/TFR.2025.3547309, provided by the authors. This work was supported in part by the Natural Environment Research Council (NERC) under Grant NE/R012229/1, in part by the Engineering and Physical Sciences Research Council (EPSRC) under Grant EP/R009953/1, and in part by the European Union (EU) H2020 AeroTwin Project under Grant 810321. The work of Raphael Zufferey was supported by Marie Skłodowska-Curie Actions (MSCA) Action under Grant 101029670. The work of Mirko Kovac was supported by the Royal Society Wolfson Fellowship under Grant RSWF/R1/18003.

(Regular Article)

ABSTRACT Existing aquatic robotic vehicles tend to be large, heavy, and difficult to deploy. This often renders them unsuitable for monitoring delicate aquatic habitats and hard-to-access areas. We present a comprehensive framework for the design and development of sailing micro aerial vehicles (SailMAVs), whose combination of flight and sailing capabilities is highly valuable for sensing missions in aquatic environments. This concept allows for quick hand-launch deployment from land, access to remote areas, rapid multipoint sampling at six locations, and easy movement between separate water bodies. Our framework places particular emphasis on the complex aero-hydrodynamic design, ensuring dual use of subsystems in both locomotion modes, which in turn maximizes performance and reduces redundant payloads. The small scale of the robots considered represents a particular challenge, in terms of both practical design aspects and the underlying physics. In addition to the hardware design, control laws are derived to allow for automated long-duration mission execution. To illustrate the proposed framework, a robotic prototype is presented, analyzed, and tested as an example. The developed design and control laws are validated in autonomous outdoor sailing missions, demonstrating the effectiveness of the framework. The prototype is further employed in remote sensing missions, demonstrating the use of SailMAVs for passive acoustic monitoring (PAM) of aquatic environments. The data obtained demonstrates the advantages of using micro aerial–aquatic vehicles (MAAVs) in biodiversity monitoring of aquatic environments with greater spatial coverage and reduced disturbance, when compared with manual methods.

INDEX TERMS Autonomous vehicles, environmental sensing, micro sailing vehicle, multimodal locomotion, passive acoustic monitoring (PAM), micro aerial vehicle, micro aerial–aquatic vehicle (MAAV).

I. INTRODUCTION

NATURAL environments are multimodal by nature, posing considerable challenges and operational constraints for single-mode robots [49]. This article addresses a form of aerial–aquatic transition for facilitation of data acquisition in aquatic environments, where acquired data is of considerable interest to inform climate models, but often challenging to acquire efficiently [29]. Swimming and flying robots [4], [17], [31], [40] can facilitate the acquisition of such data. In addition, sailing allows for locomotion at

a very low power consumption, thanks to the leveraging of wind energy. Thanks to sailing, extensive-range, long-duration data collection missions—lasting 2–6 h—become a reality.

Autonomous sailing vessels have been proposed and deployed as ground-truthing tools for satellite-based remote sensing, offering higher temporal and spatial resolution than buoys or manned ships [32]. Various prototypes have been tested for this purpose [1], [28], [38], [39]. Fully autonomous navigation has been demonstrated with a single-passenger trimaran [18], the Atlantic-crossing Avalon [13], and the commercial Saildrone, which completed missions as long as an Antarctic circumnavigation [33].

Most of these vehicles are either too large to feasibly take flight — only a few weigh under 10 kg [42]—or lack autonomy. Small-scale sailing boats employ a soft wing and mono-hull [3], [20], which makes flying capabilities more challenging to implement. Autonomous sailing boats usually struggle with maneuverability in small or shallow waters because of their dimensions [42], they cannot cross small obstacles like bridges, and they result to be costly to produce, operate, and deploy, posing challenges for environmental research. Therefore, there is strong motivation to develop small, affordable, safe, and autonomous sailing vehicles that can be quickly deployed and navigate small water bodies for extended periods.

To achieve rapid deployment, flight capability is an evident advantage, enabling a vehicle to cover long distances quickly and allowing access to water bodies where the shoreline is not accessible. Vehicles capable of both aquatic and aerial locomotion are known as micro aerial–aquatic vehicles (MAAVs) and are extremely varied in form and function [46], highlighting a wide range of strategies to capitalize on flight to improve autonomous aquatic sensing approaches. There are numerous combinations of aquatic and aerial locomotion trialed to date, being the most common grouped into multirotor, e.g., [2], [21], or fixed wing frames, e.g., [31], [36], [44]. Although the vast majority of research to date has focused on the challenges of hybrid locomotion [10], there have been some attempts at applying MAAVs for their intended sensing applications. Among these, the vast majority consist of water sampling applications using MAVs with no aquatic locomotion capability, e.g., [34], or with limited capability as demonstrated in [11]. One work that explores the design of an underwater glider with VTOL capability is also successful in measuring underwater temperature during an autonomous underwater mission [23]. Likewise, a vehicle capable of sailing and flying could perform hybrid sensing missions in which data are acquired during both flight and sailing and then combined.

This article discusses the modeling, control, design, and field testing of small-scale (less than 1.5 m wing span) aerial–aquatic sailing robots. Building on an existing proof of concept [47], where flight and sailing were demonstrated, we present here the development and testing of an enhanced demonstrator platform, suitable for long-duration outdoor operations and capable of autonomous mission execution. The platform is used for an in-depth investigation of water-surface locomotion of aerial–aquatic sailing robots, ranging from fluid dynamics to control and navigation. Thanks to extensive CFD and analytical modeling, new insight is obtained on sailing locomotion at small scales, allowing for the robot's hull geometry to be optimized. The developed models are also used to analyze the robot's sailing performance and develop novel controllers, which take advantage of a rigid sail configuration and enable the robot to sail in almost any direction with respect to the wind. To enhance the robot's applicability, a navigation unit is developed, allowing for autonomous execution of multipoint data-collection sampling missions. The developed robot is deployed in several long-duration outdoor field tests, which demonstrate its robustness, autonomous navigation, and sensing abilities. Due to the concurring requirements of the sailing and flying phases, the class of robot studied is not optimally designed for either phase, which implies unconventional properties, such as the use of rigid cambered airfoils for sailing and the absence of a keel. The small scale of the robot further differentiates it from conventional sailboats, resulting in less well-studied fluid dynamics. Our study both investigates how such a system can be deployed successfully in challenging outdoor conditions, and demonstrates the practical value of the developed concept itself as a new aquatic data sampling approach. In more detail, the contributions of this work are as follows.

1) A detailed system design of a field-worthy platform.
2) A fluid-dynamic modeling of sailing at small scales, allowing for hull geometry optimization.
3) The development of a new sailing control strategy explicitly taking advantage of the rigid airfoil sails.
4) The development of a navigation unit enabling upwind sailing and autonomous operations.
5) A proposed novel miniaturized wind sensor.
6) The validation of the proposed concept in an extensive field testing campaign.

The rest of this article is structured as follows. First, we present the conceptual design and trade-offs of aerial–aquatic sailing vehicles. Second, the detailed design and manufacturing of the main robotics parts are shown. One of the critical aspect is the design of the hull, which has been evaluated numerically. The article then discusses in depth the sailing behavior of aerial–aquatic sailing vehicles, split in two sections, covering respectively navigation aspects and outdoor field tests. Finally, we characterize the prototype in field use, and demonstrate two sensing applications.

II. LOCOMOTION OF SAILING MICRO AERIAL VEHICLES

Sailing micro aerial vehicles (SailMAVs) are multimodal robots capable of both flying and sailing, which are designed to execute repeated fly-sail-fly cycles, as shown in Fig. 1.

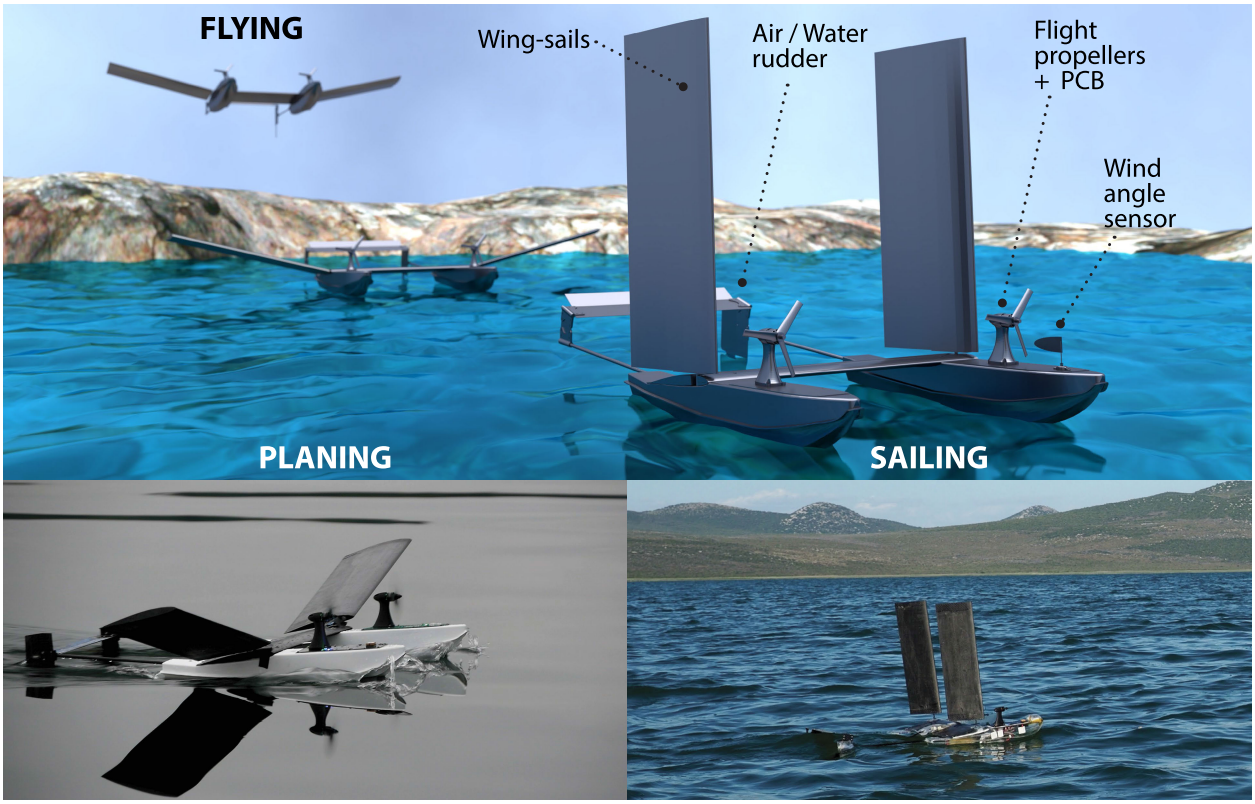

FIGURE 1. **SailMAVs are capable of flight, landing on the water, sailing, and taking off to flight.**

On a full mission, such a robot would takeoff from shore, fly to an aquatic location of interest, and land. While on the surface of the water it would sail propelled by the wind, whilst fulfilling its scientific mission. When a change in body of water is required, or an obstacle obstructs its way, the vehicle switches to flight mode again.

The specific configuration used in this study is inspired by an earlier proof of concept [47], which is enhanced and adapted (see Section III) to allow for efficient autonomous operations in outdoor environments.

A robot capable of sailing and flying poses substantial opposing constraints. Its weight needs to be minimized for takeoff, yet the aquatic environment requires adequate waterproofing as well as bulky buoyancy elements that negatively affect flight. Furthermore, a research robot should be highly modular for adjustments and continuous upgrades, which also increases its weight. The key enabler concept of hybrid robots is the reduction of complexity. An effective approach to tackle these challenges is to employ the same control surfaces for flying as for sailing, a core part of the SailMAV concept. This is possible thanks to dedicated actuators which perform the wing sail transformation. These are housed at the two extremities of the central wing and perform a 90° rotation around the longitudinal axis. This process is shown in Supplementary Video S1.

Whilst in flight configuration, the servos embedded in the sails rotate around the spanwise axis asymmetrically, thus generating roll control action; in sailing configuration, the same actuator input rotates the sails asymmetrically, positioning them with the same orientation relative to the wind. The rudder is also a shared control surface between sailing and flight: in both modes it is used to perform yaw control. The only control surface that is not used in sailing is the elevator, which is used for pitch control in flight.

By adopting this strategy where actuators and control surfaces are shared between locomotion modes, it is possible to reduce the redundant mass in each mode and thus increase overall efficiency. For example, the AquaMAV in [36] achieves a redundant payload of 29% and 20% respectively in water and air, and the SailMAV concept in [47] achieves 20% and 10%, respectively. While these values are by no means negligible, they considerably outperform systems such as MEDUSA in [11], which segregates the flight and aquatic components, and consequentially transports 39% redundant mass in flight and 42% redundant mass during aquatic operations. While more efficient, the strategy here employed is more complex to follow and requires a better understanding of the aerodynamics and hydrodynamics governing the different locomotion modes. In flight, a SailMAV largely resembles a conventional fixed-wing MAV and can be handled by off-the-shelf flight controllers, albeit with careful tuning to account for the high-authority roll control due to the entire wings rotating around a spanwise axis. The sailing phase, in contrast, is more challenging due to the small scale of such robots and the design being primarily dictated by flight requirements. We detail below a series of theoretical

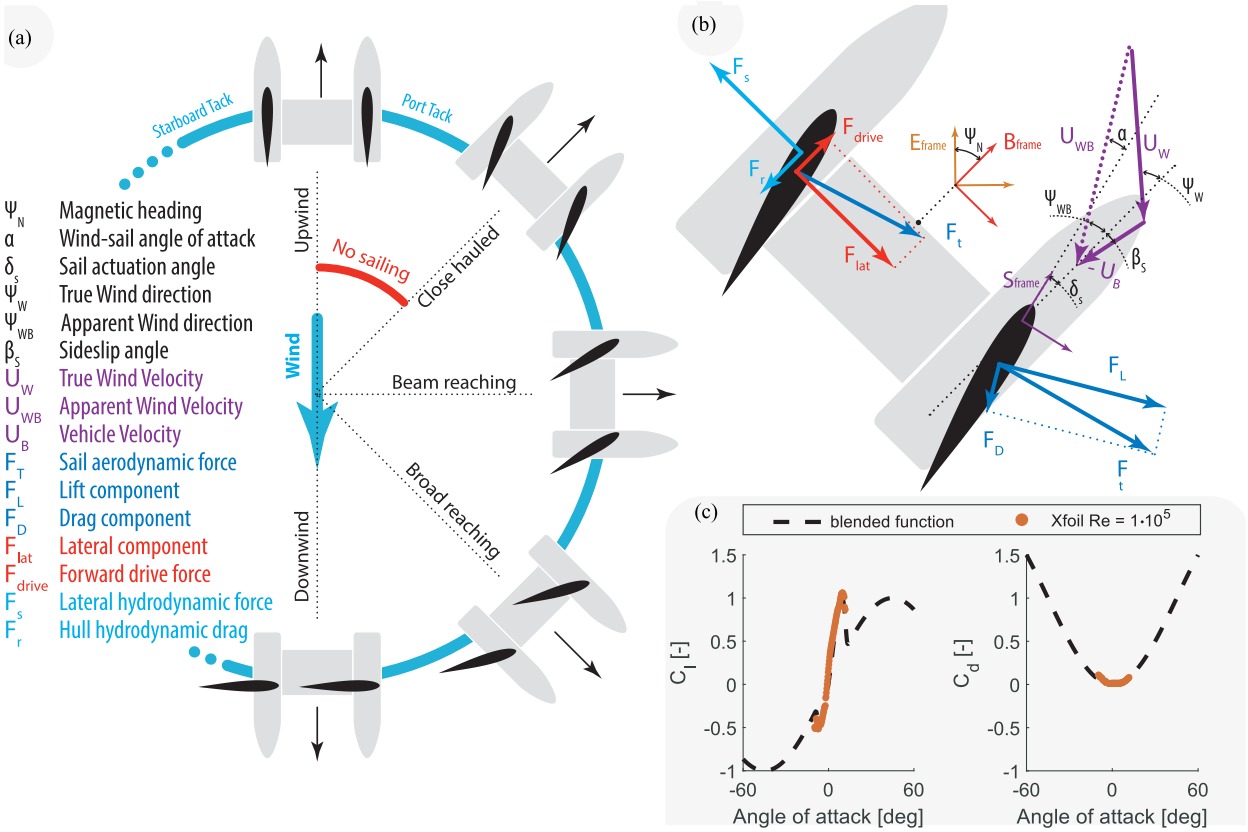

FIGURE 2. (a) Nomenclature used in sailing vessels and notation used in this publication. (b) Reference frames and forces used in describing sailing performance of SailMAVs. (c) Blended functions for lift and drag coefficients of an asymmetric airfoil: S6061. A degree 5 polynomial fit is used for C_l and C_d.

and empirical models employed used here for the design of sailing–flying robots.

A. LEVERAGING WIND: SAILING

There are a variety of analytical, empirical, and numerical tools available for the modeling of sailing vessels in the field of naval architecture. In sailing craft, the hulls produce both resistance forces and side forces as they move across the water. As shown in Fig. 2(a) and (b), the resistance forces counteract the driving force from the sails, whereas the side forces balance out the aerodynamic side forces from the sails. A good measure of performance for a sailing vessel is thus the ratio of side force to resistance force, which is loosely equivalent to a vessel's capacity to avoid drifting and travel upwind—in other words, the capacity of the vessel's hull to oppose the transverse force of the sail (desirable) to how much it opposes the sail's forward force (undesirable).

As a preliminary step in modeling sailing locomotion, we define a number of coordinate systems as follows.

1) *Earth frame (E):* North-east-down frame centered at the center of mass of the body (x=north, y=east, z=down).
2) *Body-fixed frame (B):* Right-hand frame with the x-axis aligned with the robot's longitudinal axis; B is rotated by ψ_N [in Fig. 2(b)] around the z-axis with respect to E.
3) *Sail-fixed frame (S):* Aligned with the sail; rotated by δ_S with respect to B.

A sailing vessel is subject to wind forces which are used for propulsion; however, the freestream flow experienced by the vessel also depends on its travel speed. The true wind is defined by a velocity, U_W, and an orientation in E-frame, $\Psi_W|_E = \Psi_N + \Psi_W|_B$, being $\Psi_W|_B$ further denoted as Ψ_W for convenience. The apparent wind Ψ_{WB} is the wind direction experienced by the vessel and can be computed from the true wind and body velocity, according to (1). Note that the body velocity and body orientation are not identical due to downwind drifting, which is described by the sideslip angle, given in Earth frame by $\beta_S|_E = \angle\mathbf{U_B} + \Psi_N$

$$\mathbf{U}_{WB} = \mathbf{U}_W - \mathbf{U}_B. \tag{1}$$

In practice, the apparent wind angle and speed can be measured by specialized onboard sensors, while the true wind can be calculated given an estimate of the vessel's true velocity. Further corrections are employed by sailing vessels by measuring the local water flow. However, small aerial–aquatic sailing vehicles cannot accommodate the entire suite of sensors necessary to achieve this with the current technology.

1) SAIL FORCES

In SailMAVs, the sails perform a double function in sailing and in flight, so it is preferential to use thick and rigid

profiles. This is advantageous as modern airfoil design allows for greater performance than classic fabric-based sails [9]. Another advantage of rigid wings is the fact that their shape will not change due to creep and is less likely to be damaged, an obvious advantage for autonomous vehicles. Moreover, lift and drag forces can be easily calculated based on available data, and procedures already exist to estimate induced drag and other effects, which are difficult to obtain for a membrane wing. On the other hand, fabric-based sails do not suffer from stall, or can avoid stall by being manipulated in a continuous fashion, instead of relying on discontinuous control laws, such as the one shown in Section V.

One intrinsic difference between sailing and flying is that the wing sail in sailing needs to operate over a much wider range of angles of attack, as driving force is generated mostly by the lift component when traveling more upwind, and by the drag component when traveling downwind [see Fig. 2(a)]. A consequence of this mode of operation is the necessity to have data on the poststall behavior of airfoils, information that is scarce in the literature. This behavior can be estimated assuming that the wing behaves as a flat plate poststall, a justifiable assumption after flow separation. The $C_{l\,\mathrm{flt}}$ and $C_{d\,\mathrm{flt}}$ of a flat plate can be derived from the potential flow equations, which make a good approximation of stalled airfoils. A function that takes into account both the low angle of attack range (obtained with the vortex panel method [8]) and the approximate poststall behavior, which can be obtained by blending a polynomial approximation of the former component with the latter. Blending is performed in the intervals of $\delta_+ = [\alpha(C_{l\,\max}), \alpha_{\max}]_{\mathrm{vpm}}$ and $\delta_- = [\alpha_{\min}, \alpha(C_{l\,\min})]_{\mathrm{vpm}}$ (as estimated by vortex panel method) via bounded weighted averaging, e.g., pairs of functions such as $w_{n\,\mathrm{vpm}} = \sin^2(\pi/2\delta)$ and $w_{n\,\mathrm{flt}} = \cos^2(\pi/2\delta)$. This results in analytically defined blended functions for C_l and C_d, which can be seen in Fig. 2(c) for the particular case of the S6061 airfoil used on the reference platform.

2) HULL FORCES

The hull forces are here modeled using semiempirical approaches used for boats, modified to account for the case of hybrid flying–sailing vehicles. For instance, unlike typical sailboats, SailMAVs are unlikely to have a keel to generate side forces and prevent drifting, as a keel increases longitudinal drag to the extent that it will prohibit flight, takeoff, and landing. Moreover, the scale of SailMAV is considerably different to that of boats and not all the involved physics scale equally, making it impossible to design experiments which simultaneously conserve all the involved physics. These physics are the flow inertial forces, flow viscous forces, gravity, and surface tension, which can be defined in terms of Froude's, Weber's, and Reynolds' nondimensional numbers, defined in this context as in (2), where u is the free-stream velocity, g the gravity, l a length scale, ρ the fluid density, σ the surface tension, and ν the fluid's kinematic viscosity

$$\mathrm{Fr} = \frac{u}{\sqrt{gl}}, \quad \mathrm{We} = \frac{\rho u^2 l}{\sigma}, \quad \mathrm{Re} = \frac{ul}{\nu}. \tag{2}$$

For the reasons pointed above, even though we follow well-known semiempirical approaches to model the hull forces, some care is taken to devise our own expressions or to use numerical calculations where necessary. The total resistance of a hull shape moving through water can be expressed as in (3), according to the well-known ITTC-78 model [6]

$$C_{\mathrm{tot}} = (1+k)\, C_f + C_w \tag{3}$$

where C_f is the frictional resistance coefficient, C_w the wave resistance coefficient, and $(k+1)$ the form factor. Viscous resistance dominates at low speeds, while wave resistance becomes more significant at higher speeds. The two components are predominantly dependent on the Reynolds number and the Froude number, respectively. While the first can typically be estimated empirically [25] as in the following equation, the second is typically determined experimentally or using experiment-derived empirical formulations:

$$C_f = \frac{0.075}{(\log \mathrm{Re} - 2)^2}. \tag{4}$$

There is significantly less agreement in the literature on the wave resistance and available analytical methods are complex [26]. Instead, empirical expressions are generally obtained experimentally for specific platforms [25]. Nonetheless, C_W is largely independent of scale (hence Re) – this means that experiments on scaled models can be conducted to determine the coefficient value for full-sized vehicles through Fr similarity.

The form factor depends on the geometry and accounts for the viscous resistance of the hull form. It is independent of Re and Fr but nonetheless highly complex. Values for k are often found experimentally, but various empirical approximations have been proposed. We use the following equation, which is specifically obtained for a double-hulled configuration [37], and where Δ_0 is the hull's displacement:

$$(1+k) = 3.03\left(\frac{l}{\Delta_0^{1/3}}\right)^{-0.4}. \tag{5}$$

Based on slender body theory for a body moving through a flow at an angle (corresponding to leeway), the side force can be determined from [27, eq. (6)], where $d_{\max}$ is the draft and Φ is the leeway angle (or sideslip/drift angle)

$$F_s = \frac{1}{2}\rho u^2 \pi \Phi d_{\max}^2\, l. \tag{6}$$

B. ACCELERATING TO FLIGHT: TAKEOFF

SailMAVs employ a takeoff strategy akin to seaplanes, where the robot accelerates horizontally on the water surface, using the propellers, until sufficient lift is generated for takeoff. As a SailMAV accelerates along the water surface, it experiences buoyancy, as well as hydrodynamic and aerodynamic drag and lift. The vehicle begins its movement in the displacement regime, where its weight is mostly supported by buoyancy, its velocity low, and wave drag is the dominant force. In this regime, the flow is dominated by the Froude

number [ratio of inertial forces and external force field in (2)], with the maximum drag found for Fr $=$ 0.5. As speed increases beyond this, hydrodynamic lift is generated, pushing the vehicle upward and reducing wave drag. Ultimately, the vehicle reaches planing, where hydrodynamic lift and skin friction drag are dominant, before it finally takes off and transitions to flight. In the planing regime, the flow is dominated by inertial and viscous forces and the Reynolds number becomes important.

Analytical and empirical estimates derived by Savitsky [35] are commonly used to evaluate hull drag and planing speeds. As Savitsky produced a variety of works and mistakes are commonly made on the units used, the exact equations are compiled in Supplementary Section A, in SI units.

Solutions to the system of equations shown in Supplementary Section A can be found in Fig. 3(a), where the evolution of the drag force F_D with the Fr number is shown for different hull geometries. These geometries are of constant weight and $l \cdot b$ but varying l/b (representing hulls with equal buoyancy but different aspect ratio). The drag force is calculated by solving (1) and (2) in Supplementary Section A, and assuming the CG position to be 0.5 l, the height of the thrust vector to be 0.5 b, and the deadrise angle to be zero. It is shown that the planing drag of low l/b hulls is smaller and reduces sharply at lower speeds, indicating that such hull geometries will reach planing much faster. More importantly, the maximum drag produced during the transition period is lower, requiring less thrust and thus a lighter propulsion unit. It is thus trivial to relate F_D/Δ_0 to the Thrust/Weight ratio of the aircraft, a common design parameter, and define a target for $\max(F_D/\Delta_0)$ for the choice of l/d. However, hull operation in sailing must also be considered in terms of side force F_s to drag force F_D ratio calculated using (3) and (6): an estimate of a hull geometry's performance in keeping a heading during sailing. As shown in Fig. 3(a), hulls that perform better in planing will have a lower sailing performance, generating higher drag for the same amount of side force and drifting more than other geometries.

Even though Fig. 3(a) clearly shows the opposing design constraints experienced by planing–sailing hulls, there is no clear optimal configuration on which a design decision can be made. We propose a process to find an optimal slenderness ratio l/d for such hulls as follows.

1) Taking into account the guidelines in [5] and [14], generate baseline designs of constant $l \cdot b$ (constant draft), and varying l/b (varying slenderness ratios).
2) Iteratively solve the equations in Supplementary Section A for each geometry, and find scaling factors C_i for which $\max(F_D) = 0.4\Delta_0$, being 0.4 the target thrust-to-weight ratio required at takeoff.[1]
3) Calculate the sailing performance ratio F_S/F_D for the obtained scaled geometries, using (3)–(6), and select the geometry that best performs in this metric.

By adhering to this process for a SailMAV, as detailed in Supplementary Section B, we can investigate design parameters such as the form factor l/d and the beam loading coefficient C_Δ. Fig. 3(b) shows the results obtained when evaluating step 3 of this process. Based on these results, a rough hull geometry with ($l/b \sim 7$) is selected, before fine-tuning more detailed geometrical parameters using CFD in Section IV, and taking manufacturing constraints into consideration in Section III.

III. PROTOTYPE DESIGN AND MANUFACTURING

The SailMAV reference platform studied possesses a structure based around a double hull linked by a rigid central wing. An early demonstration of this concept has been presented in [47], albeit with physical and engineering limitations, which made it unsuitable for real-condition missions. Most of the design and manufacturing methods are entirely different, and are presented in this section.

A. STRUCTURE DESIGN

As SailMAVs are envisioned for long-distance and efficient flight, thanks to their fixed-wings configuration, implementing a highly streamlined structure is particularly important. The added aerial–aquatic complexity of the design makes this task challenging. As these robots are for now intended to function as research prototypes, modularity, repairability, and upgradability are crucial aspects. These combined design objectives led to the structure illustrated in Fig. 4(a).

1) HULL MANUFACTURING

Manufacturing a thin-walled hull with prototyping methods is difficult. While 3D printing has become ubiquitous in robotics fabrication, it remains poorly suited to creating large and strong hollow structures. Blow molding is the process employed in the manufacture of bottles and containers, in which high-pressure air forces the walls of a cylindrical, base container, to conform to a mold. Unfortunately, this is a large series process and prohibitively expensive for prototyping. Vacuum forming, on the other hand, also produces thin, formed shells. The equipment needed for this method is much simpler, and the molds can be 3D-printed or CNC-cut in dense epoxy foam. Vacuum forming, however, cannot produce revolution shapes. Therefore, SailMAVs' hulls are split horizontally into two concave shells, see Fig. 4(a).

The bottom half of the hull features a rising keel that generates hydrodynamic lift at low speeds, a shallow deadrise angle to reduce wave impact, a step which facilitates takeoff, and an angled stern for planning performance. The smoothness of the mold is important as it directly impacts water friction. The top half of the hull is bonded to the bottom half along a lip which extends outward. It features two large openings: the front printed circuit board (PCB) opening and the back wing

[1] A relatively large thrust ratio, comparatively to conventional seaplanes (0.1 T/W), is necessary to overcome surface waves at this scale.

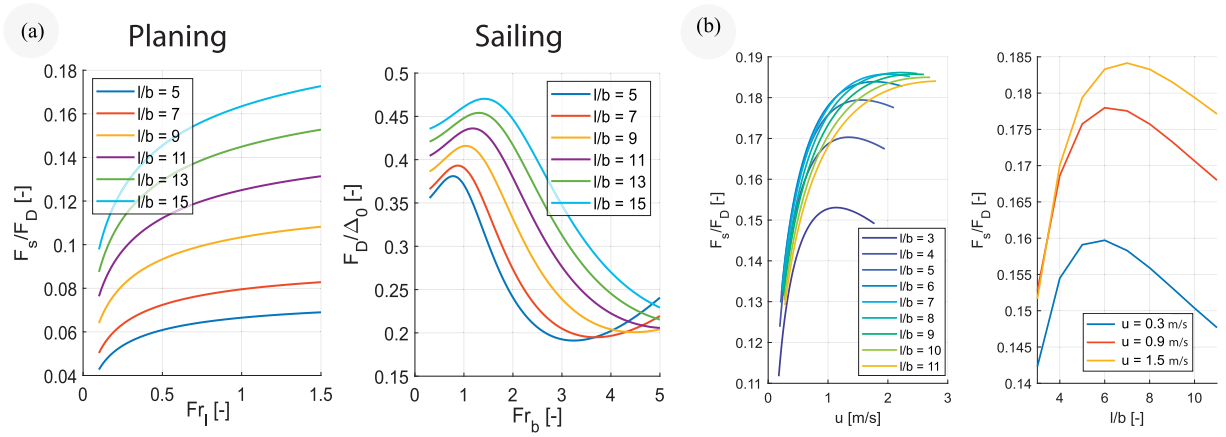

FIGURE 3. **(a) Side force to drag force ratio over the range of $0.1 < Fr_l < 1.5$ during planing for hull geometries of different l/b and $\max(F_D/\Delta_0)$ over Fr_b. (b) Side force to drag force ratio over velocity for varying geometries.**

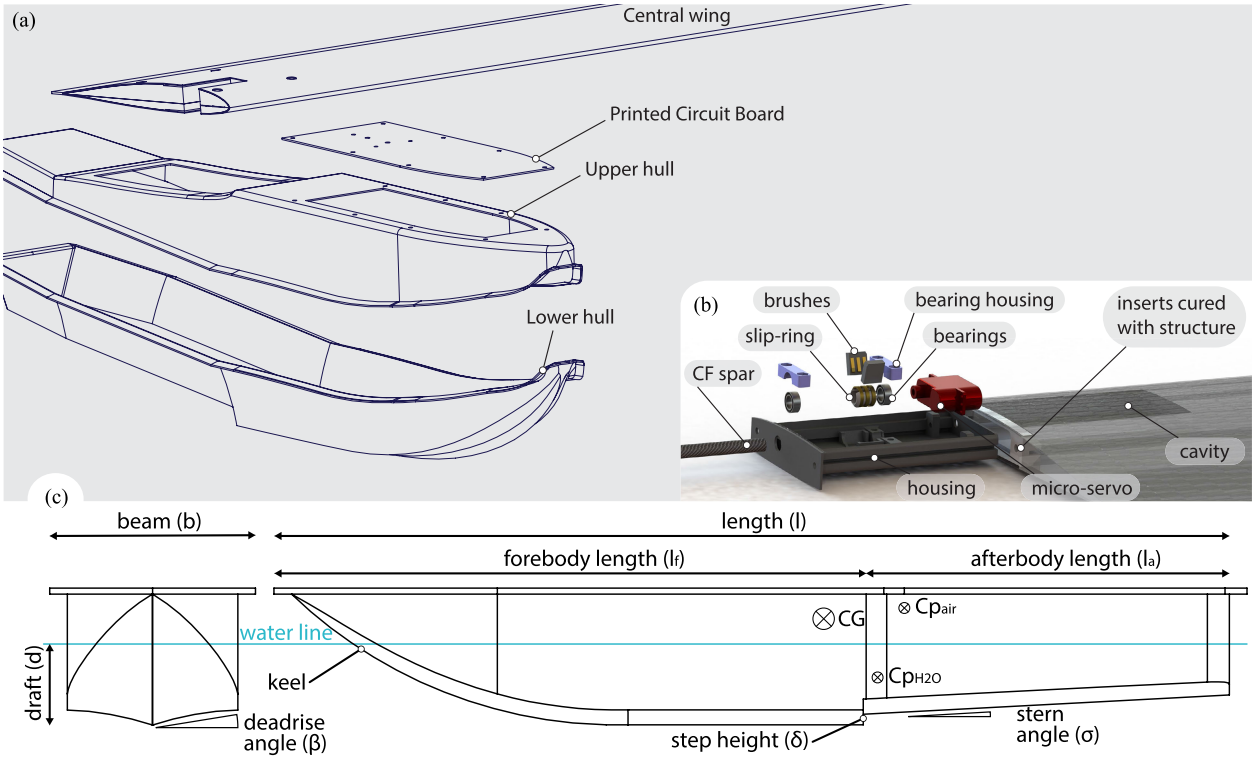

FIGURE 4. **(a) Exploded structure view. (b) Sails embedded actuation design. (c) Schematic of hull design parameters.**

opening. Even though these are not submerged by design, they are regularly in the splash zone or submerged in extreme conditions, so they are both sealed with compression silicone foam seals. Such conditions can for example be found in Supplementary Video S2.

2) CENTRAL WING

Besides functioning as a lifting surface, the central wing functions as a structural element by linking both hulls. It is manufactured from a machined polyimide foam core and resin-infused carbon-fiber skin, and extends over both left and right hulls, to the outer edge of both hulls. Thanks to this topology, the central wing is attached in four points to each hull, resulting in a rigid body group. This connection method effectively covers a large opening at the top of the hull, from where access to internal components and maintenance are possible. The edges of this opening are layered with a laser-cut silicone foam sheet for a waterproof seal, compressed by the four attachment screws.

B. SAILS DESIGN

The sails are actuated around their connecting spar for both roll control in flight and wind-driven propulsion in sailing. This form of actuation has its drawbacks, namely in flight, the direct drive of the sails can generate a very large control action in roll, leading to inadequate control. However, as shown in [48], using a single actuator for both these functions is extremely effective in reducing redundant payload (up to 50% reduction). Thus, the sail angle-of-attack actuation is performed by a servo embedded in the wing, creating a requirement for a very accurate servo that can perform the required level of control within the $\pm 4^\circ$ range used for roll control. On the other hand, the range of actuation needs to be suitable for sailing: ideally, a 180° range is needed. Another constraint is that the actuator needs to be protected from water and thus fit in the sail airfoil which has a 16 mm maximum thickness.

The embedded sail actuation is implemented through an actuation module fitted in a cavity located at the inner extremity of the wing, as shown in Fig. 4(b). This actuation module is bound by a 3D-printed housing piece that slides into the cavity along rails that are embedded in the core structure during curing. A carbon-fiber tube mechanically links the sail to the folding actuator and allows for power lines to be passed through the middle. To prevent entanglement of these lines during operation, a custom slip ring is used to transmit power and signal to the servo. This is achieved with a pair of bearings, a 3D-printed housing for three brass rings which fits on the spar, and two pairs of brushes which contact the rings. The two actuation modules weigh 27 g each and have operated for more than 80 h in wet environments without ever sustaining water damage, even surviving capsizing.

A final design concern is the aerodynamic loading on the sails, which provide up to 78% of the lift. Even though the load-bearing capacity of the carbon fiber (CF) spar or the sail in itself is of no concern, the roll servo needs to be able to counter the pitching moment acting on it during flight. This moment is minimized by positioning the spar at the 1/4th chord.

C. HULL DESIGN

The hull plays a key role in the transition to flight; however, its design is a nontrivial process, with multiple constraints deriving from flight stability, planing stability, drag in flight, and sailing performance. The key geometrical parameters for hull design are shown in Fig. 4(c). Conveniently, hull design for water takeoff was well studied in the 1950s, and some general design rules have been compiled in the literature [5] and [14], which served as a guide in this study. However, there are some unique aspects of hull design for the particular case of small-scale sailing–flying vehicles, which we elaborate here.

First, the proposed SailMAV is significantly smaller than seaplanes and even than most models used in experimental studies, so the influence of spray is much more preponderant. In fact, at smaller scales, spray generation happens at lower Weber numbers, generating less droplets but more cohesive jets of spray which have a greater impact on propellers and lifting surfaces.

Second, the water clearance is typically low for SailMAV prototypes, making ejection of spray onto the propulsion units and aerodynamic surfaces likely. Using strut-mounted hulls, as on seaplanes, is not an option for keel-less small-scale sailing–flying vehicles due to the danger of capsizing when sailing crosswind. This leads to tighter constraints on roll stability and wing clearance, so that stern waves can easily reach sufficient height to wash over the craft's tail. On the other hand, the low clearance has the positive effect of increasing aerodynamic lift and hastening the transition to planing as well as takeoff.

Further considerations arise from the combined design constraints for flight and sailing. The positions of the CG, CP, and step, for instance, need careful consideration. Conventional planing hull design dictates that the CG should be located along the 10° line fore of the step [Fig. 4(c)] to maintain stability, while CP in flight is classically placed at 1/4th of the wing chord, enforcing a stern-leaning wing position as shown in Fig. 4. Another consideration is drag in flight and in sailing. While it is advantageous for planing hulls to have large beams, this is disadvantageous for sailing and flight, where more slender bodies are preferable.

Finally, the use of a keel, while advantageous for sailing, is not compatible with planing due to the large keel volume that remains in the water even if planing is reached. While a planing hull is not an issue in downwind sailing, drift becomes prohibitively high when traveling crosswind or upwind. This problem could be addressed by developing a deployable keel; however, additional actuators should be avoided at the considered scale. The approach we take is to design hulls such that a compromise between sailing and planning performance is reached. Such a compromise is achieved by studying key geometrical parameters such as l/d using the process described in Section II-B.

D. ELECTRONICS

The robot is controlled by a Pixhawk5 flight microcontroller running the px4 firmware [24]. Featuring an ARM M4 running at 180 MHz, it outputs the signals to the eight actuators and reads all onboard sensors. It is connected in the left hull to a power and signal PCB, custom-designed for the robot. This board interfaces with the central wing bus (CWB), a 15-line link to the right hull. In addition, the folding actuator as well as the tail and sail servo are also connected to the board. The CWB is made from marine-grade silicone-coated wire that can resist harsh conditions. Note that the cables extremities connect straight into the PCBs, without being exposed to the outside. Two 450 mAh batteries, one in each hull, are connected in parallel to maintain mass symmetry. They supply 16 V to the electronic speed controllers (ESCs) and a voltage regulator, which independently powers both the

controller and the actuators. Both the 16 V and regulated 5 V lines are distributed on both hulls via the CWB.

1) STRUCTURAL ELECTRONICS

PCBs are typically manufactured with a glass fiber laminate (FR4) which possesses high strength-to-weight ratio. We propose the use of PCBs as electronics support as well as mechanical sealing component.

Both the right- and left-side PCBs seal the top front part of the hulls. This brings several major benefits. First, the PCB is fixed to the top of the hulls *component-side inside*, which significantly reduces the probability of water contact should there be water ingress in the hull. Second, overall weight is reduced, thanks to the lack of a stand-alone lid plate. Third, the PCB itself does not require additional fixation inside of the hull.

The 6 mm edge of the PCB is empty of electronic components to serve as a seal area. A silicone seal ensures waterproofing between the hull and the PCB. The backside of the board is coated with an epoxy layer to avoid any shorting. The motor mounts are fitted on the backside with three through-hole screws.

2) PROPULSION

A brushless motor and electronic speed controller pair is included in each hull and each powered directly by the battery included in the same hull. The VBAT line that is included in the CWB is used purely to balance both batteries, thus carrying very little current during standard operation. As shown in Fig. 5(c), the motors are fixed to a 3D-printed mount which is fixed on the outward facing side of the PCB. Electrical contact is ensured with spring-loaded connectors, allowing for quick replacement. Waterproofing is ensured via compression of a silicone seal between the mount and the PCB.

The choice of motor and propeller is made by performing static thrust tests on a force balance, for various 2400–2800 Kv motors and 4'' tri-blade propellers. With the obtained data, it is possible to make predictions on the power usage during cruise and thus predict the flight range of the robot.

3) SENSING

The sensors necessary for flight control and navigation are included on the PCB; these are all compatible with the off-the-shelf PX4 firmware. A total of three sensors are located onboard, sharing data for navigation purposes. A GPS receiver with barometer ensures stable flight in outdoor tests and offers room for expansion toward waypoint-based control. The SAM-M8Q GNSS antenna module (*U-blox, Switzerland*) is placed on the outward facing side at the head of the PCB, for clear sky view and clearance from the water when sailing. Waterproofing of the contacts is ensured by covering the exposed edge with a low viscosity resin. Wind velocity is obtained from a pitot tube. To this end, the SDP3x differential pressure sensor is mounted on the PCB directly, with two tubes linked to the pitot tube on the central wing.

To sense wind direction, we develop a novel miniature and waterproof sensor. Fig. 5(b) shows the wind direction sensor mounted on the left hull. It is based on the AS5048b hall-effect sensor, which measures the magnetic field angle from an external magnet. The sensor itself is placed on the inward facing side of the PCB to be protected from the environment; however, the wind arrow and magnet are placed directly on the outer side so that they are exposed to the wind. The arrow is coupled to the magnet via a bonded 3D-printed component, and the magnet is allowed to rotate freely at very low friction by fitting inside the inner ring of a ceramic zirconium dioxide bearing which is unaffected by magnetic fields. The sensor is placed on the left hull, far from other avionics, as the magnet has a strong interference effect on magnetometers. A custom driver was written for PX4 compatibility with the wind sensor and integrated in the open source code included in the Supplementary Material.

4) ENVIRONMENTAL SUITE

A sensor suite that collects environmental data is included in the left hull and interfaced with a microcontroller unit (MCU) that forwards the data to the flight controller via MAVlink. Alternatively, an SD-card slot on the left hull directly stores the collected data.

The BME280 - Bosch Sensortec atmospheric sensor is included on the inward facing side of the PCB to measure atmospheric pressure temperature and humidity. The measurement is isolated from the inside space of the robot by overlaying the sensor with a silicone tube that passes through a hole on the PCB made for this purpose. The mouth of the tube is curved downward to avoid water ingress.

Another separate temperature sensing component (TSYS01 - TE Connectivity) is placed at the bottom of the hull with direct contact to the water through a hole for water temperature sensing. This board is bought off-the-shelf and includes a high-accuracy reference voltage regulator, and physical insulation of the sensor from the rest of the board to achieve a calibrated accuracy of $\pm 0.1\,^{\circ}\mathrm{C}$.

For certain missions, an acoustic sensing payload—the AudioMoth device (Open Acoustic Devices, Southampton, U.K.)—was included. However, this component operated independently and was not integrated with the main system.

IV. NUMERICAL EVALUATION OF HULL PERFORMANCES

Hull performance of the preselected geometry obtained in Section III-C was evaluated through numerical studies. This geometry is shown in the technical drawing in Supplementary Section C, it has a form factor l/d of 6.85 and operates at beam loading coefficients C_{Δ} of [10.7, 12.9] depending on the payload. Its main distinguishing feature is a double chine; while the upper one diverts the spray at low speeds, the lower one diverts the spray at higher speeds. Numerical simulations were performed to fix a limited number of design parameters, and evaluate the performance of this hull in planing and in

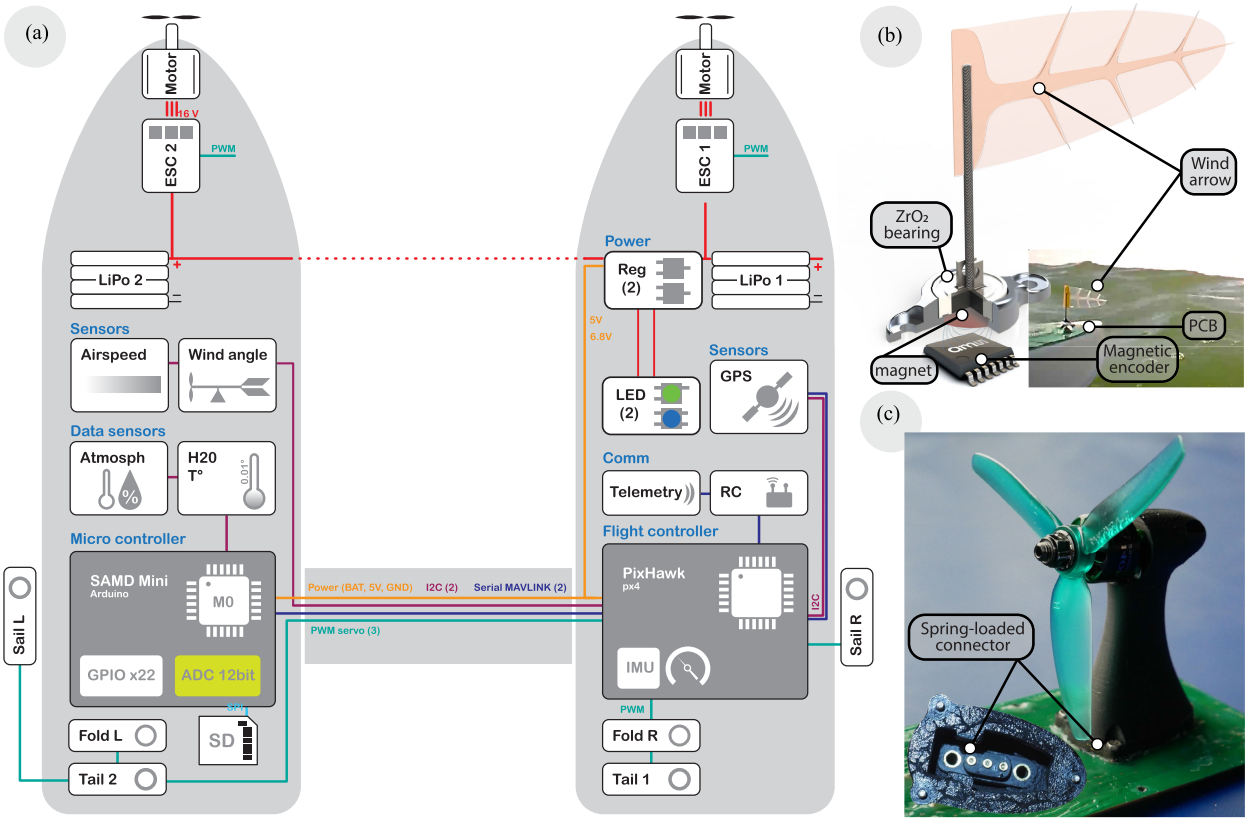

FIGURE 5. (a) Distribution of electronics components and actuators on SailMAV. (b) Custom wind direction sensor. (c) Quick disassembly propulsion unit.

sailing. Details on the physics solved and numerical methods used are shown in Supplementary Section D.

A. PLANING CONDITIONS

It is found that porpoising, a high-amplitude oscillatory motion of heave and pitch, can occur for this geometry for Fr $>$ 1.5, and that the horizontal position of the center of gravity has a strong effect in amplifying or reducing this effect. This is to be expected, as the center of gravity position will directly influence the hydrodynamic stability margin. As shown in Fig. 6(a), the system becomes more stable as the center of gravity is moved forward. This indicates that the hydrodynamic center of pressure is positioned toward the bow of the hull, likely an effect of the high forebody length to total length l_f/l of the hull being studied. The selection of the CG position thus needs to not only be informed by the stability condition in flight, given by the static margin (h), but also by the stability in planing during takeoff.

Simulation results for planing conditions are shown in Fig. 6(b), where the maximum C_D is reached at Fr $=$ 0.5, a characteristic of dragging hulls subject to wave drag. At higher Froude numbers, hydrodynamic lift is generated, pushing the hull into planing conditions, where the lift to weight ratio approaches 1. The skin friction drag force is also shown to plateau as the aft-body bubble shown in Fig. 6(c) forms. This bubble formation is characteristic of stepped hulls and reduces drag at high speeds and can also be seen in experiments such as in Supplementary Video S3.

The step size at the bottom of the hull has a major influence in the aft-body bubble formation and planing stability. Two different step heights δ are thus evaluated: a step height to beam ratio of 10% (high-step) and of 5% (low-step). Flow features are found to be mostly identical; however, the high-step geometry is found to porpoise at higher Fr numbers, while the low-step geometry is not. This is due to the stronger suction created after the step, leading to excessively high trim angles and moving the hydrodynamic center of pressure further back. As shown in Fig. 6(b), the trim angle of the low step hull reduces after the aft-body bubble reaches its maximum growth at Fr $\sim$ 2, improving trim stability. Moreover, the low-step geometry is found to produce lower drag through the entire range of Froude numbers simulated, likely because the smaller step geometry has higher displacement, making it float higher in the water at lower Fr. Due to the aforementioned advantages, a lower step height is used for the prototype used in Section VII.

B. SAILING CONDITIONS

By changing the flow's incidence angle in yaw, one can mimic the sideslip angle experienced by SailMAV when it

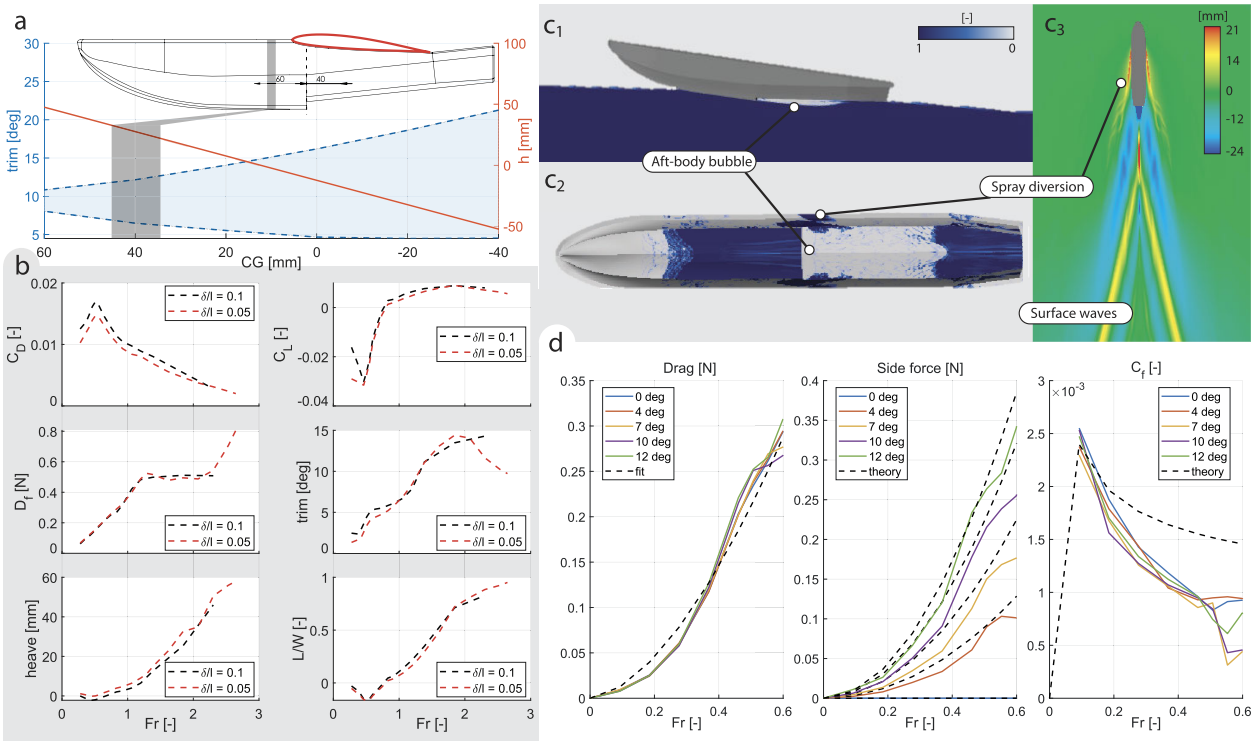

FIGURE 6. (a) On the left axis, the upper and lower porpoising limits as a function of CG position. On the right axis, the variation of static stability margin for a fixed wing and tail configuration. (b) Drag and lift coefficients, skin friction drag, pitch, heave, and hydrodynamic lift to weight ratio of a SailMAV hull geometry, as a function of the Froude number. (c1)–(c3) Side and bottom view of volume fraction of water, and top view of water-surface height for Fr = 3. (d) Drag force, side forces, and skin friction drag coefficient of a SailMAV hull geometry in sailing at different sideslip angles, as function of the Froude number. Nondimensional numbers are calculated with $l = 480$ mm, $g = 9.81$ m/s^2, $\rho = 997$ kg/m^2, and $S = 0.036774$ m^2.

sails upwind under drift. In this study, the domain width needs to be increased to account for the off-center wake. This setup does not take into account the interaction between the two hulls of the considered configuration; however, this is not expected to be significant at the small yaw angles studied here.

The drag force, side force, and skin friction drag coefficient obtained from the simulations are shown in Fig. 6(d). For sideslip angles of up to 12°, the wave drag varies very little with the sideslip angle and the friction coefficient only slightly decreases with the angle, due to separation occurring on the downstream side of the hull. Furthermore, we show here that the theoretical/empirical expressions defined in Section II-A only slightly overestimate the side force of the hull, while considerably overestimating the skin friction drag at higher Froude numbers. As the variation of wave drag with incidence angle is below 10% from the range of angles and speeds considered, a least-squares fitting is used to find an exponential function for wave drag: $D_w = 0.679\text{Fr}^{1.6803}$. This function is employed in Section V to predict sailing performance metrics.

V. SAILING ENVELOPE

Due to payload limitations, a SailMAV has considerably less information available for sailing control than most autonomous sailing vessels. While the latter measures apparent wind speed and direction, global position and velocity, as well as apparent hull velocity, SailMAV can only rely on apparent wind direction, global position, and its velocity components as output from the EKF data fusion in the flight controller. Nevertheless, it is still possible to devise control strategies and path planners that achieve autonomous waypoint navigation. To achieve this, however, SailMAV's operational envelope must first be defined in terms of viable upwind angles, drifting angle,s and travel speeds. It is especially important to be able to predict the sailing performance of such prototypes when traveling upwind. Although sailing boats cannot travel directly upwind, they can advance against the wind by sailing in beam reaching to close-hauled range [see Fig. 2(a)]. By repeatedly zigzagging while keeping the wind in this angle range, they can advance upwind. Note that this holds for true wind angles: apparent wind angles can reach much smaller values.

The theoretical foundation needed to calculate the operational envelope of SailMAV in sailing mode has been laid in Section II. First, the sail-related forces are calculated, which depend on the control input to the sails and should provide an optimal forward travel force—here denoted as sail strategy. Such strategies relate the measured apparent wind angle Ψ_{WB}, directly measured by the wind sensor in body frame, to a

target sail angle δ_s. Ψ_{WB} is defined as 0 when the wind is directly upwind and has a discontinuity at 180° or −180°. Strategies such as (7a) can be found in the literature [15] and [43]; however, these are not necessarily optimal for rigid wing sails

$$\delta_s(\Psi_{WB}) = \frac{\pi}{4}\text{sign}(\Psi_{WB})(1-\cos(\Psi_{WB})) \tag{7a}$$

$$\delta_s(\Psi_{WB}) = \begin{cases} 0.4924\Psi_{WB} & \Psi_{WB} \in [-180, 0] \\ 0.9728\Psi_{WB} & \Psi_{WB} \in [0, 70] \\ 0.4735\Psi_{WB} & \Psi_{WB} \in [70, 180]. \end{cases} \tag{7b}$$

The poststall expressions devised in Section II-A are characterized by two lift maxima, so it is expected that an optimal function will take advantage of these two maxima by having a discontinuity in the crosswind to upwind travel region, where lift becomes the dominant component of the driving sail force. A simple procedure is to calculate the driving C_{Ft} and side C_{Fs} force coefficients for a set of sails and choose sail angles that maximize the driving force, or the driving force to side force ratio. Here, we choose to maximize the driving force, as the $C_{\text{Ft}}/C_{\text{Fs}}$ strategy presents little change when compared to the max(C_{Ft}) one. Note that the driving and lateral forces are defined in Fig. 2 but here referred to as C_{Ft} and C_{Fs} for conciseness.

Fig. 7(a) presents the smooth strategy in (7a) and the max(C_{Ft}) strategy. The latter presents two discontinuities, one at +90° and another at −48°, which indicate the wind angles at which it becomes more advantageous to take advantage of the second C_l maxima. The different angles at which these discontinuities occur are a consequence of an asymmetric airfoil being used. An adapted version of the max(C_{Ft}) strategy is also presented, which corresponds to a piecewise linear fit of max(C_{Ft}). This strategy takes into account SailMAV's actuation limitations of $\delta_s \in [60°, -60°]$, as evaluated in Fig. 2 and skips the discontinuity at negative wind angles as this small section at shallower sail angles provides little performance gain.

Fig. 7(b) and (c) show the drive force and side force coefficients applied by one of SailMAV's wings given three different sailing strategies. It is shown that the smooth function consistently underperforms when compared with max(C_{Ft}) strategies, especially at more upwind conditions, when an airfoil's maximum C_l point can provide greater lift at much lower drag, leading to greater driving forces and much lower side force. Furthermore, SailMAV's actuation limitation has a greater impact when traveling downwind when the sails cannot reach 90°, but also in the $70° < \Psi_{WB} < 90°$ interval. This shows that as soon as the robot reaches beam reaching position, the use of rigid wing-sails can have a considerable advantage. Finally, as previously discussed, there is little loss in performance when the shallow negative angles section is skipped by the piecewise fit function. This function is provided in (7b)

$$U_{WB}\cos(\Psi_{WB}) = U_B\cos(\beta_S) + U_W\cos(\Psi_W)$$
$$U_{WB}\sin(\Psi_{WB}) = U_B\sin(\beta_S) + U_W\sin(\Psi_W)$$

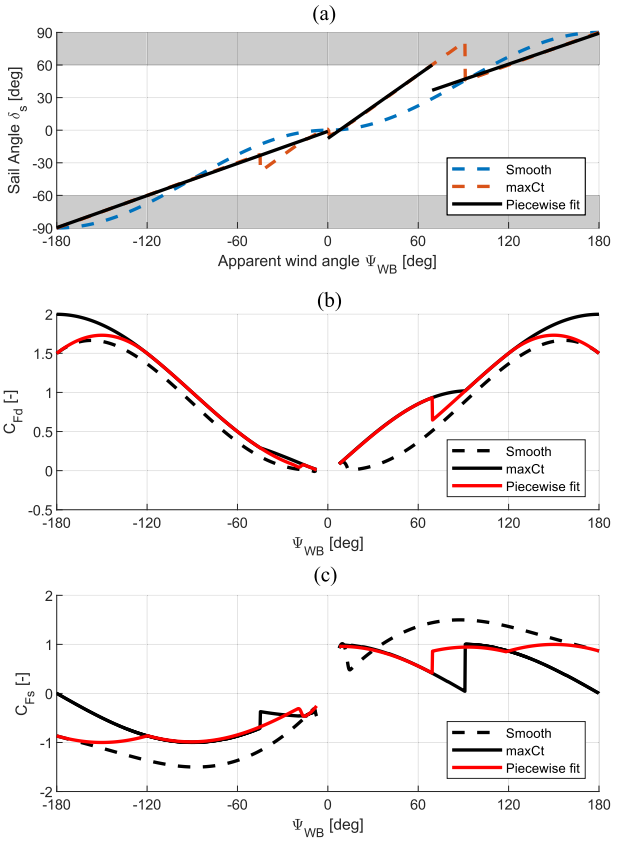

FIGURE 7. (a) Sail angle as a function of apparent wind angle for smooth sail strategy [15], [43], maximum drive force strategy, and 60° bound piecewise fit. Gray area indicating angles beyond the servo's operational range. (b) and (c) Sail resulting forces in the body frame of reference (drive and side force coefficients) for multiple sail strategies: smooth, maximum drive force, and 60° bound piecewise fit.

$$2F_{r\,\text{hull}}(\beta_S) = F_{t\,\text{sail}}(\Psi_{WB}) + F_{t\,\text{sail}}(-\Psi_{WB})$$
$$2F_{s\,\text{hull}}(\beta_S) = \begin{cases} F_{s\,\text{sail}}(\Psi_{WB}) + F_{s\,\text{sail}}(-\Psi_{WB}) \\ \qquad\qquad \text{if} \quad \beta_S < 0 \\ -F_{s\,\text{sail}}(\Psi_{WB}) - F_{s\,\text{sail}}(-\Psi_{WB}) \\ \qquad\qquad \text{if} \quad \beta_S \geq 0. \end{cases} \tag{8}$$

Combining the sail forces calculated above and the hull forces obtained in Section IV, the system of equations (8) can be used to make predictions on travel speeds and drift angles. These equations calculate steady-state sailing conditions by performing the force balance of hull and sail forces. While sail forces are a function of the apparent wind angle Ψ_{WB}, hull forces depend on the apparent water-current angle, which here is assumed to be equal to the drifting angle β_S. This assumption is equivalent to considering underwater currents negligible.

The solution of this system of equations allows for predictions to be made on the robot's travel speed and drift angles. As shown in Fig. 8, the max(C_{Ft}) strategy yields high performance gains throughout, and especially in upwind movement.

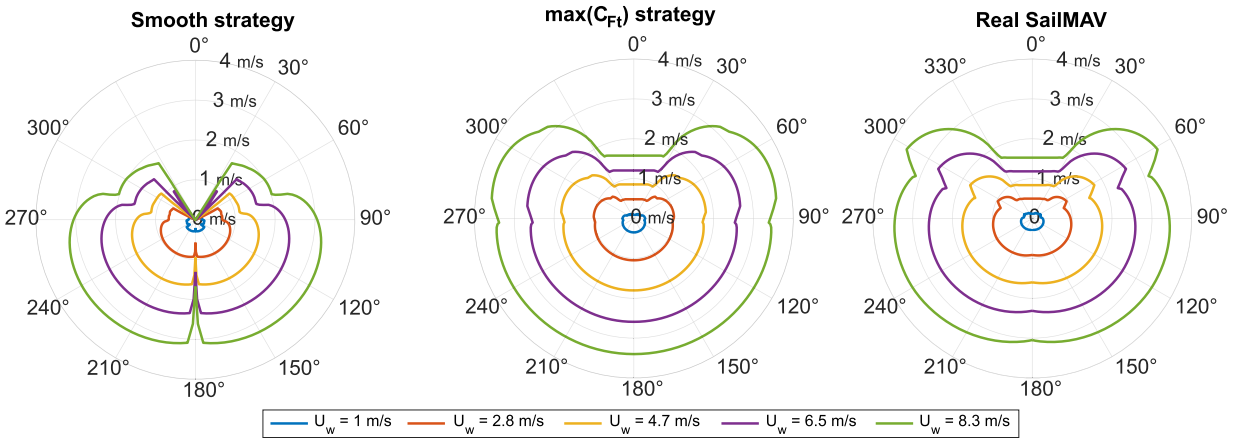

FIGURE 8. **Polar plots of travel speeds at different global wind speeds and different apparent wind angles Ψ_{WB}, for the 2 sail strategies and for the SailMAV (taking into account limitations of the actuators).**

Starting at wind speeds of 5 m/s, it is even predicted that SailMAV can travel the fastest at 60°, hinting that it will be able to efficiently tack and move upwind.

In order to visualize the tacking performance of the different strategies, it is easier to evaluate the component of U_B projected on the upwind direction. Fig. 9 shows this value normalized by true wind speed for the two different sail strategies and the real SailMAV. It is shown that SailMAV has an optimal tacking angle of 50°, at which it travels upwind fastest. When sailing 50° to a true wind of 5 m/s, the robot is subject to a drift angle of 18.4°, so it will be traveling only 68.4° to the wind. At 44° heading and the same wind speed, the robot will drift 27.5°, effectively traveling 71.5° to the wind. The lack of a keel is clearly visible here. While most sailing vessels can tack at ±45° effective heading, SailMAV achieves a maximum of ±68.4°.

There are several simplifications in this analysis that have an effect on the results. For instance, the sails are in each other's wake when traveling cross-wind, decreasing generated driving force. Moreover, even though the model predicts that at Fr $>$ 0.5 the drag coefficient decreases, this is most likely not the case. In fact, the wind action on the sails introduces pitching and roll moments on the robot which force the hulls deeper into the water and prevent planing. This produces a twofold effect: increased drag forces, slowing the robot beyond model predictions; and increased lateral force which can decrease drift. Simulating these effects requires more complex simulations of all the degrees of freedom of the robot.

VI. AUTONOMOUS SAILING

The water-surface controller is based on a switching approach. The underlying concept is that depending on the condition the robot perceives itself to be in, it will activate or deactivate different components of the navigation and control framework. This will allow the robot to undertake different types of missions and locomotion modes, according to Section VI-B, and to successfully deal with varying environmental conditions, such as changing winds.

Once the robot has landed on water, it will enter either the sail mode or the propeller-assisted locomotion. In case the wind condition is favorable for safe sailing, as specified in Section VI-A, the robot will enter the sail mode and activate the sailing controller.

The source of the desired heading information depends on the strategy set for the mission by the user, which can be either a preset waypoint strategy or an angle with respect to the Earth reference frame. Sails and rudder are adjusted in order to best follow this angle. This is presented in Section VI-C.

To augment the navigation and control system's functionalities, supplementary features have been integrated, beyond the fundamental sailing capabilities. These comprise course-keeping, waypoint skipping, halt, as well as activation and deactivation of the propellers. Additionally, to address the challenges posed by the water environment and to conserve energy, a silent mode was developed. This mode temporarily blocks the sails, reducing noise and allowing the robot to operate quietly during certain periods of time.

The controller command strategy for both sails and rudder changes as required by the switching mechanism, and uses onboard measurements to determine how the controller should act in a particular situation. This is discussed in Section VI-D.

A. ASSUMPTIONS AND LIMITATIONS

Prior to presenting the sailing algorithms, we need to consider a number of preliminary aspects, which influence the control framework design and the resulting performance.

1) The controller requires GPS data to function to provide necessary geolocation data.
2) The lack of a keel leads to substantial drift, particularly when sailing in crosswind or upwind conditions. The controller continuously adjusts the direction to align

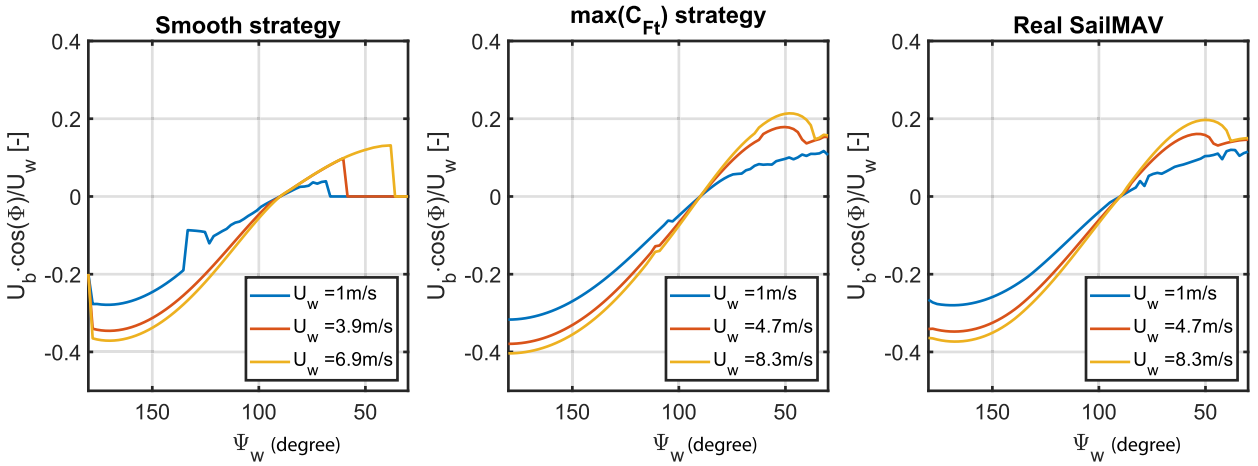

FIGURE 9. Advance to true wind direction Ψ_W (in degrees) normalized by true wind speed, as function of true wind Ψ_W for different true wind speeds.

with the target. As it does not compensate for drift, this can result in less efficient trajectories.

3) Wind orientation is detected by the custom wind angle sensor described in Section III-D. The sensor measures apparent wind angle direction Ψ_{WB} which is fed to the sail's controller. An exponential moving average filter is applied to decrease the sensor's oscillations and obtain a smoother and more reliable sail output. This comes with the drawback that the controller can be slow to adapt to very fast changes in wind direction, as shown in Supplementary Video 4, where a wind change coincides with a tacking maneuver and causes both hulls to become submerged under a strong pitching moment.
4) The ability to navigate in both air and water is highly dependent on weather conditions. Specifically, the range of wind speeds that allow both flight and sailing is a crucial factor to consider.
5) The performance of the controller is limited by the lack of wind speed information. The reliability of the pitot sensor in providing accurate airspeed information is contingent on the wind flow direction being aligned with the motion direction.

B. SWITCHING MECHANISM

A simplified version of the switching process is illustrated in Fig. 10. As can be seen in the algorithm, the controller takes input of weather conditions and navigation strategy from the ground control station deciding the locomotion mode on water surface (sailing or with propellers).

Upon landing of the vehicle, the water-surface mission commences. At the onset of every mission, the ground control station transmits an estimated wind speed, acquired from the wind speed equipment, to the vehicle. If this value exceeds a given threshold, sail-based navigation becomes a risk for the platform, potentially resulting in flipping and loss of control of the robot. In this case, the sails will remain folded down after landing, and the propellers will be activated for completing the mission. Following extensive experimentation with varying wind conditions, a threshold wind speed safety limit of 25 knots was established. Beyond this limit, field tests have demonstrated that sailing on the designated test platform becomes hazardous. In the occurrence of advantageous weather conditions, the sailing locomotion mode will be initiated. This will involve the upward folding of the robot's wings to serve as sails, while the propellers will be deactivated, enabling the robot to be propelled by wind energy.

C. WAYPOINT STRATEGY

Autonomous environmental survey missions typically require waypoint tracking capabilities to cover the key points of the freshwater resource to be mapped. Waypoint missions were set according to the overall wind conditions that the robot would face during the duration of the mission and especially based on the ecological aim of the mission considered. This may for instance include navigating around sensitive and protected areas, but also in areas of high human activity. Each waypoint is described with its latitude Φ and longitude λ, as is also the GPS position feedback information. The controller's task is to ensure the robot follows the waypoints. During the mission it calculates the bearing θ and distance d from the current position (Φ_t, λ_t) to the next waypoint (Φ_n, λ_n) according to the conventional geolocation formulations

$$\begin{aligned} x &= \cos(\Phi_n)(\Delta\lambda) \\ y &= \cos(\Phi_t)\sin(\Phi_n) - \sin(\Phi_t)\cos(\epsilon_n)\cos(\Delta\lambda_n) \\ a &= \sin^2(\Delta\Phi/2) + \cos(\Phi_t)\cos(\Phi_n)\sin^2(\Delta\lambda/2) \\ \theta &= \text{atan2}(x, y) \\ d &= 2 * R * \text{atan2}\left(\sqrt{a}, \sqrt{1-a}\right) \end{aligned} \tag{9}$$

with R denoting the Earth radius.

The controller operates to guide the robot toward the target as long as the distance surpasses a threshold ($d > d_{\min}$). Upon reaching the target, the waypoint is updated. Subsequently,

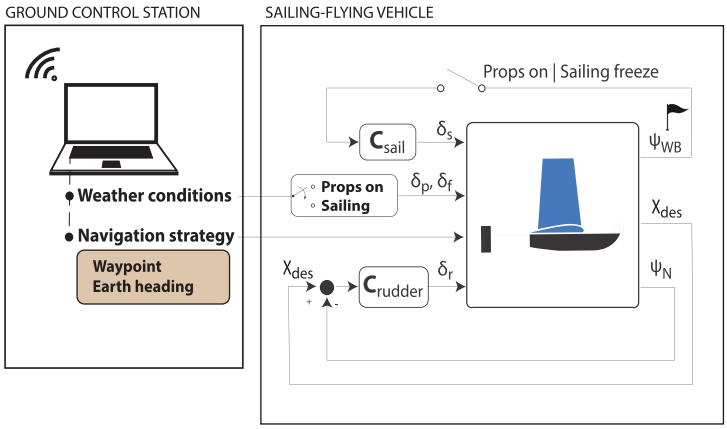

FIGURE 10. **Schematic of switching approach used for control and navigation. Input signals: δ_p, propellers: δ_f, folding mechanism: δ_s, sails: δ_r, rudder. Output signals: δ_r.**

Algorithm 1 Switching Logic: Determine Actuator Inputs

Control station: *Weather conditions, sailing strategy,* Ψ_W, V_W
Input measured: *GPS position, Attitude,* Ψ_{WB}
if *Sailing* **then**:
    $\delta_f = 1$ {Fold up wings}
    if *Waypoint* **then**
        $d = distance(Waypoint_n, GPSposition)$ {Distance from MAV to target}
        if $d > d_{min}$ **then** {The des. waypoint has not reached yet}
            $\theta = bearing(Waypoint_n, GPSposition)$ {The angle (NED) between MAV and target}
            if !*Tacking* **then** {No Tacking}
                $\chi_{des} = \theta$
            else
                $\chi_{des} = \Psi_W + i * \chi_t, \quad i = [-1, 1], \quad \chi_t = 50$ {Tacking maneuver}
        else if $(n < number\_waypoints)$ **then** {Else: des. waypoint has reached, If: is the last one?}
            $n++$ {Update Waypoint}
            $\theta_1 = bearing(Waypoint_n, GPSposition)$ {Compute 1st bearing, to discriminate for tacking}
            $Tacking = |\Psi_W - \theta_1| > \zeta$ {Check if the first bearing is in no sail-zone}
    $\delta_p = 0$ {Switch off propeller's motors}
    $\delta_s = f(\Psi_{WB})$ {Sail input according to formulation 7b}
else
    $\delta_p = 0.1$ {fixed 10 % propeller's propulsion, high enough to move}
    $\delta_s = 0$ {Set sails/wings to 0 position} x
$\delta_d = f(\chi_{des}, \Psi_N)$ {Rudder input according to formulation 10a}

the initial bearing (θ_1) is computed, determining whether the robot will adopt a tacking strategy. This occurs only if the difference between θ_1 and the ground control station's true wind direction (Ψ_W) remains below a threshold (ζ). When tacking is inactive, the desired heading (χ_{des}) aligns with the bearing. Conversely, if tacking is engaged, the desired heading zigzags around the true wind direction (Ψ_W) with an angle (χ_t). Values for χ_t and ζ are established as per Section V.

The aforementioned waypoint algorithm follows a sequence of procedural directives outlined in Algorithm 1, while further elaboration is available in Suplementary material (S.E).

D. CONTROL DIAGRAM

As previously noted, the inputs to the robot in sailing mode consist of the rudder and sails, updated every 0.01 s.

The rudder controls the heading of the vessel by adjusting the difference between the desired heading and the current yaw attitude. An extended Kalman filter (EKF) is used to estimate the true orientation of the vessel using measurements from onboard sensors. The EKF is implemented in the open-source autopilot PX4 used in this study.

Although the EKF provides reliable heading estimation, it does not account for drift effects that may influence the direction of motion. One method to account for drift is to use vessel velocities relative to the local robot reference frame.

However, this method is challenging due to noise and uncertainty in velocity measurements and water wave oscillations that introduce measurement noise.

The rudder's operation relies on a closed-loop feedback control mechanism, aiming to minimize the disparity between the desired heading and the real heading. The actual heading is referenced to the Earth's frame of reference (Ψ_N). Rudder adjustments are governed by a mathematical equation, with a restriction when the robot deviates from the target by over 90°. This constraint ensures the autonomous sailing robot navigates proficiently and successfully throughout its mission

$$e = \chi_{\text{des}} - \Psi_N \tag{10a}$$

$$\delta_r = \begin{cases} \sin(e), & \text{if} \quad \cos(e) \geq 0 \\ \text{sign}(e), & \text{if} \quad \cos(e) < 0. \end{cases} \tag{10b}$$

With respect to sail control, its design is exclusively contingent upon the orientation of the apparent wind. This approach is based on the principle of optimizing the use of the available wind to propel the robot. The direction of the wind is continuously monitored and used to determine the optimal angle of the sails, which in turn maximizes the robot's forward speed and overall efficiency.

In (7a) and in previous work on sailing–flying robots [15], [43], a strategy was proposed that only leverages downwind power, thereby limiting the capability to sail upwind beyond a certain angle utilizing sail propulsion alone.

The newly proposed strategy described in formulation (7b) capitalizes on the shape of the airfoil to enhance the sailing capabilities of the platform. By leveraging the airfoil shape, the platform's ability to sail upwind is significantly improved, as outlined in Section VII-A. This strategy presents the potential for the platform to operate autonomously regardless of the wind direction and mission objectives.

VII. FIELD EXPERIMENTS

To demonstrate the effectiveness of the control strategies and design concepts presented in this article, an extensive field testing campaign was conducted in several locations in the U.K., Switzerland, and Croatia, in fresh and brackish water. The specific trials here presented were conducted in the Round Pond in Hyde Park (51.505826, -0.183498) and Lake Vrana (43.909619, 15.550942) in Croatia. Aerial footage of one of these missions is shown in Supplementary Video S5. A list of physical parameters describing the dimensions of crucial components as well as weight and inertial properties are summarized in the table present in Supplementary Section B.

We present in this section several experiments conducted to demonstrate the resilience of the proposed design, as well as the performance of its sailing strategies and controllers. These experiments were conducted in outdoors uncontrolled environments, where SailMAV was dropped to a water body and let to autonomously perform a sailing mission of predefined waypoints. Furthermore, the experiments bring insights into the use of Sailing-MAVs for environmental mission, in terms of travel efficiency and data obtained. The data here presented is obtained from the vehicle's flight controller logs. While information such as the vehicle's global position and pose are logged by the flight controller (FC) firmware, the environmental data and other information pertaining to sailing (e.g., the measured wind direction) are logged via custom-defined MAVLink messages generated in the microcontroller (μC) and parsed in a custom FC module.

A. AUTONOMOUS SAILING PERFORMANCE

Two sail control laws are introduced for SailMAV in Section V, one of which considers its wing geometry and aims to maximize the driving/propulsive force generated by the wind. Fig. 11(a) shows SailMAV attempting the same waypoint mission twice, using first a generic smooth wing control law, and afterward the dedicated max(C_{Ft}) law. The robot completes the mission successfully both times, achieving different conditions for skipping the first set point. In the first attempt, it cannot reach the target 15 m margin from the set point; however, it eventually accumulates enough drift that the target heading surpasses the value of the initial heading +90° and the first set point is skipped. In the second attempt, the robot can maintain a closer effective heading to the wind direction, reaching the 15 m margin and proceeding to the second waypoint. It is shown that by using the max(C_{Ft}) sail strategy, the robot can travel on average 12° further upwind. While the target heading varied between 70° and 50° to the true wind, the robot achieves only 84°, which is in accordance with the expected drift angle of ∼10° at this heading range.

Concerning sailing speed, it is shown in Fig. 11(b) that there is no significant improvement from using the max(C_{Ft}). In fact, SailMAV underperforms when compared with the steady-state sailing model for both sail strategies, which is a clear consequence of the simplicity of this model. The most significant effect not being taken into account is the fact that pitching and roll moments applied by the sails make the hulls sink deeper into the water and produce more drag. In fact, the drag model used predicts that the drag coefficient decreases at Fr $>$ 0.5, as the hull starts transitioning into planing. However, the increased downforce applied by the sails prevents this from happening, by forcing the hulls down into the water. This is especially visible in Fig. 11(c), where the downwind hull frequently is fully immersed when the robot travels cross-wind and in Supplementary Video 6, where the negative pitching moment induced by the sails opposes the hydrodynamic lift generated by the hulls. This is not the case when traveling at more upwind angles (40°–70°) where the higher volume of the hull's forebody is sufficient to keep it from pitching forward excessively (as observed in Supplementary Video S7). This is an indication that the negative impact of the lack of actuation range in the wing (±60°) is twofold. First, as predicted by the model [Fig. 7(b) and (c)], the drive force is reduced, and second, the side force is increased. As this side force not only acts toward drift but

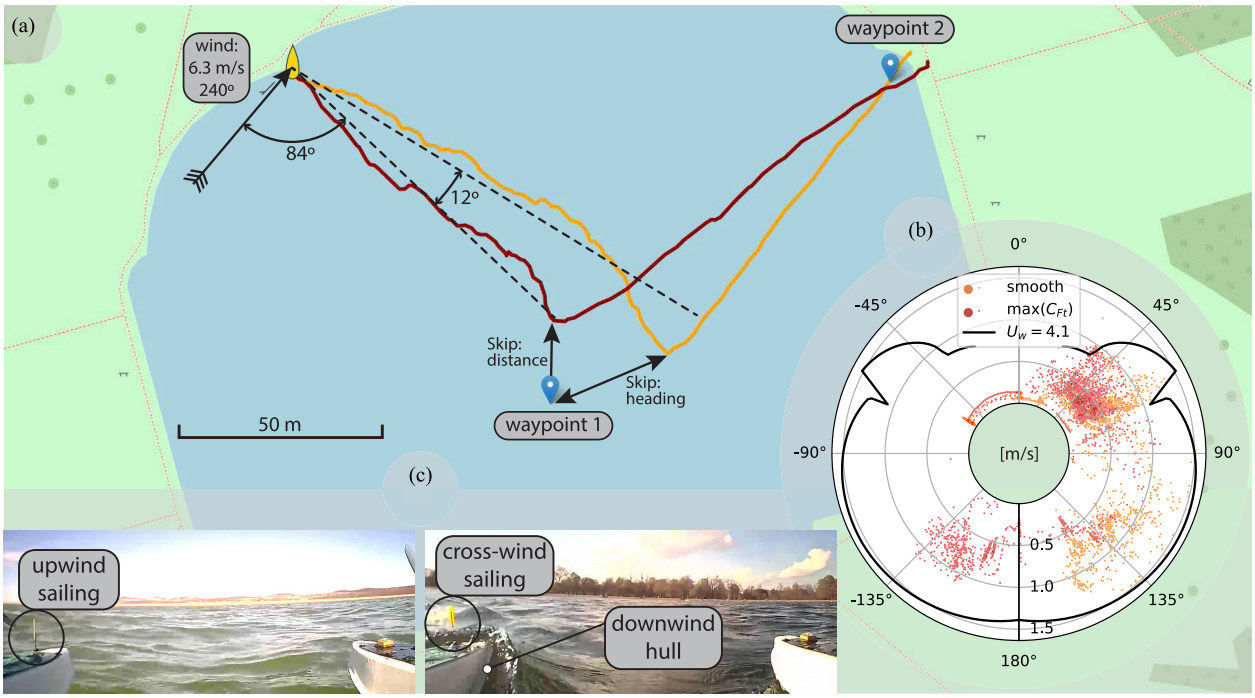

FIGURE 11. **(a) Mission overview in the Round Pond in Hyde Park, U.K. In yellow a mission executing a generic smooth sail control function and in red the same mission executed using the max(C_{Ft}) strategy. Both missions are performed within a 25 min interval with equivalent average wind speeds. (b) Polar plot of the ground speed in radial axis and apparent wind direction Ψ_{WB} in the angular axis. (c) Still frames taken from an on-board camera when the robot is traveling upwind and downwind at ∼1.3 m/s.**

also induces a strong roll moment, it further contributes to increasing drag and consequently reducing the sailing speed.

Fig. 12 demonstrates a single waypoint mission located 14° upwind at mission start. As the waypoint is within the ±45° range right from the start, the path planner transitions immediately to the tacking strategy and sets the heading at 50°. The robot then holds this heading, achieving an average effective heading of 57°, showing slightly better tacking performance than the predicted 63°. For the subsequent two tacks, it achieves only 64°–71° upwind effective headings due to a temporary decrease in wind speeds. This is especially visible at the third tack (footage shown in Supplementary Video S7) when the wind speed drops below the minimum tacking speed ∼3.5 m/s and SailMAV looses some advance to the wind.

It is shown in Fig. 12(a1) how the recorded travel speeds are within the expected range, especially in the tacking range. Even though this experiment is conducted at lower speeds than in Fig. 11, it is shown that the robot consistently reaches similar speeds of over 1 m/s in the upwind region, showing that sailing-induced moments are not as impactful in this region. A maximum speed of 1.55 m/s is reached in this mission, which corresponds to a Froude number of 0.71. In fact, the maximum speed reached by the robot was of 2.2 m/s during a period of 10.2 m/s average wind, corresponding to a Froude number of 1 (footage of this test is included in Supplementary Video S8). In this region, the hulls start to produce positive hydrodynamic lift, leading to reduced resisting side forces Fs_{hull} and thus yawing downwind. This sharply reduces the speed, before enough speed is built up again for the robot to yaw back upwind, creating a periodic oscillatory yaw motion. This behavior is shown in Supplementary Video S9, and needs further consideration so that the relative position of the sail to the hull can be used to stabilize this motion without jeopardizing pitch stability in flight and in planing.

Fig. 12(b) shows the robot approaching a waypoint after accumulating considerable drift. As the condition to initiate tacking is deactivated, it overshoots as it tries to reach a target which is too upwind. This results in the heading set point moving further and further to port side, eventually turning the robot's starboard side to the wind, and performing a tacking maneuver. The same happens as the robot overshoots a second time and soon after reaches the 15 m margin of the waypoint, meeting the conditions to proceed to the next one. This process is inefficient as the robot faces very upwind throughout the entire tacking period and moves slower than when an active tacking strategy is used. Nevertheless, this passive behavior can be interesting for small sailing robots with very limited computation and sensing options.

B. ENVIRONMENTAL SENSING WITH SailMAVs

As mentioned in Section III-D4, SailMAV has an integrated environmental sensing payload which measures, among other variables, water and atmosphere temperatures. This is a critical measurement, as the heat exchange between large bodies

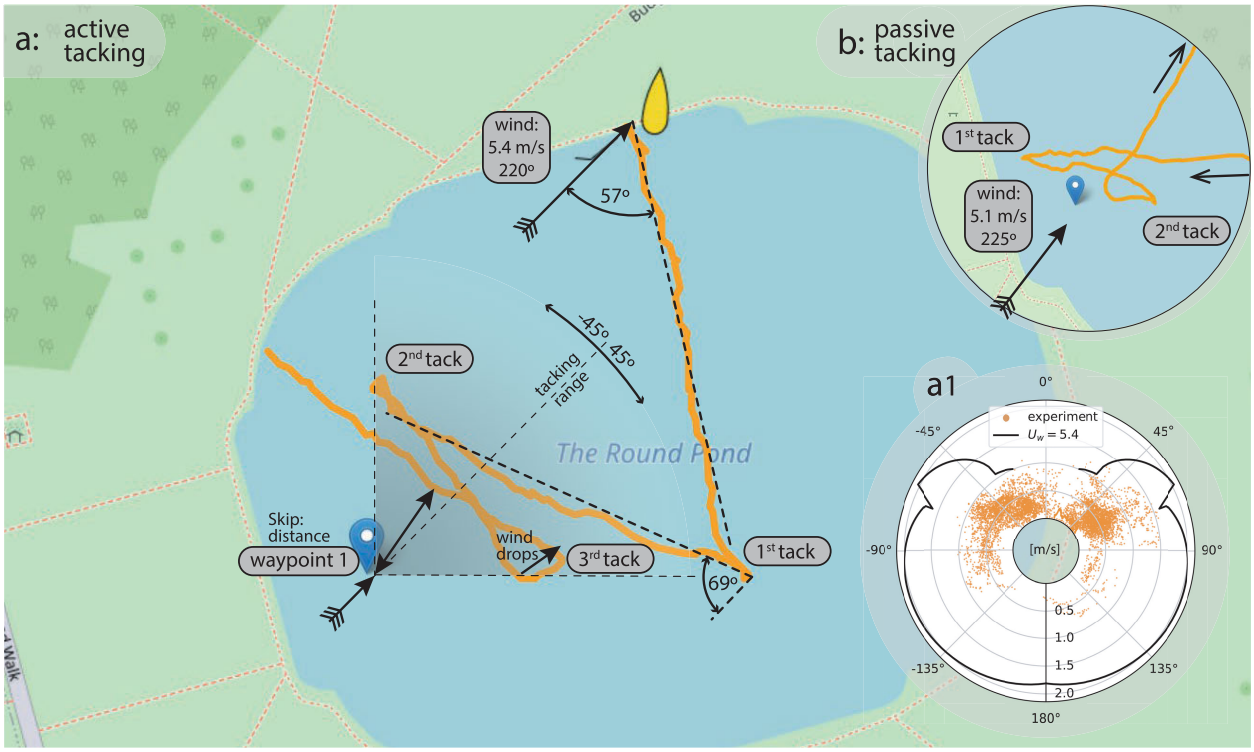

FIGURE 12. **(a) Mission overview in the Round Pond in Hyde Park, U.K., showing the global position tracking of the robot overlayed with key performance metrics and the wind-centered limits at which tacking occurs. (a1) Polar plot of the ground speed in radial axis and apparent wind direction Ψ_{WB} in the angular axis. (b) Detail on passive tacking occurring in a different mission where no tacking strategy is active.**

of water and the atmosphere has a crucial impact on weather patterns. Moreover, these measurements normally need to be performed at higher accuracy than what is possible with sensors measuring infrared radiation. SailMAV successfully conducted missions lasting up to 6 h, relying on two 450 mAh batteries that were nearly depleted by the end, with a remaining charge between 50% and 25%.

Fig. 13(b) demonstrates a mission in which water and atmospheric temperature were recorded. The gradients encountered are in fact not spatial gradients but temporal ones derived from changes in the air temperature. This claim is supported by the lake's small spatial scale and the fact that changes in atmospheric temperature are caused by air currents traveling faster than the robot itself. However, in longer missions, decoupling spatial and temporal gradients is no easy task, which will likely require novel data processing methods to be developed. Nevertheless, the potential scale (in both time and space) of the data that can be acquired with SailMAV during sailing makes this type of sensing an interesting option for aquatic environments.

SailMAV was also equipped with microphones and hydrophones for a testing campaign in Croatia. Fig. 13(a) reports on these tests, during which audio data was recorded for future processing. This study aimed to utilize SailMAV's inherent quietness during the sailing mission stage to perform passive acoustic monitoring (PAM) of the Vrana Lake. PAM in ecology involves using sound recorders to survey environments, with signals of interest typically extracted using species classification algorithms or acoustic indices [12], [41]. During this study, it was found that SailMAV surveys found higher species richness and call abundance than classic stationary surveys, something which has previously been found in a comparison of point counts vs line transect surveys [45]. This result may be because SailMAV was able to access not only bankside areas, but also the open water body, habitats which are likely to contain different species. We also found high site dissimilarity owing to species turnover between data collected using moving and stationary techniques, again likely due to the difference in habitats accessed. This suggests that stationary and moving approaches to data collection may be complementary.

In total, 2263 min of surface and underwater acoustic data were recorded during six individual deployments on sequential days, and BirdNET [16], a deep artificial neural network, was used for bird species classification. A total of 87 species were recorded during this period, 35% of the bird species known to inhabit Lake Vrana. The study also showed how species richness in nonprotected areas of the lake is low, being generalist species such as cormorants and swans mainly found there. On the contrary, the ornithological reserve was found to be inhabited by a variety of birds of prey and herons, among others.

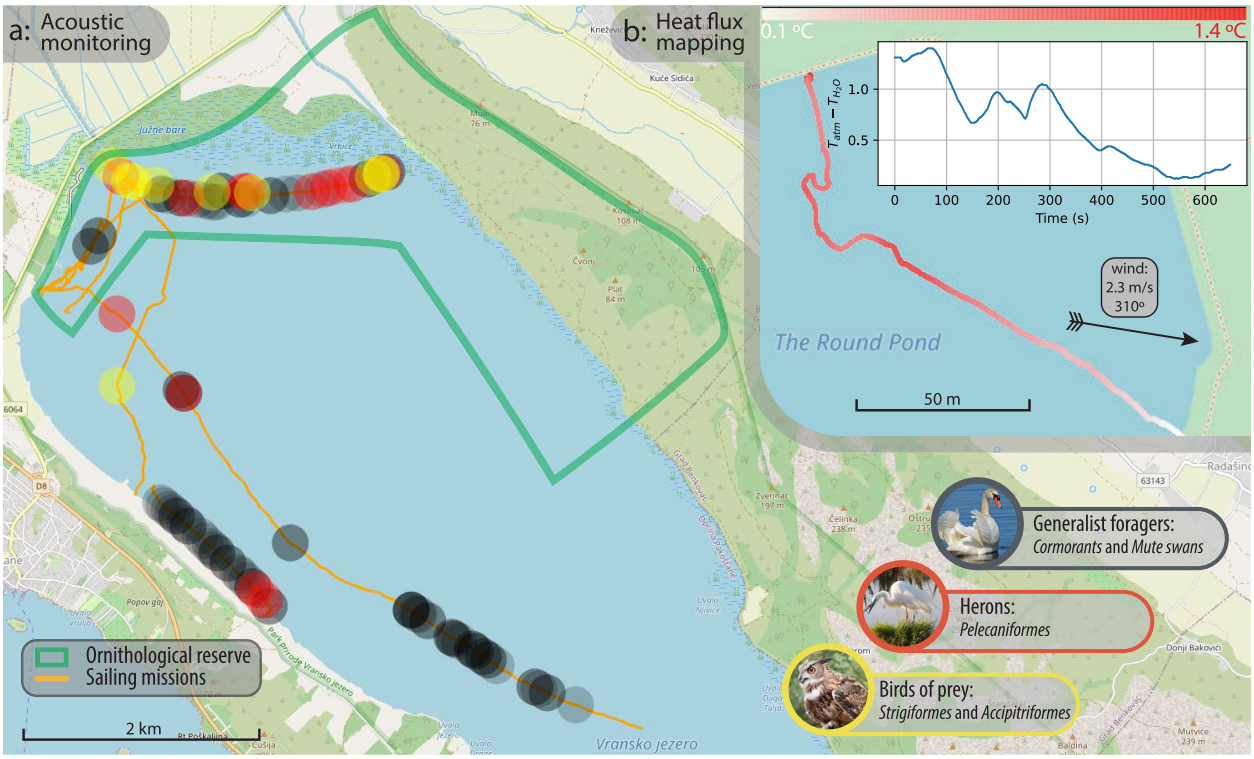

FIGURE 13. **(a) Summary of various sailing missions in Lake Vrana, Croatia, inside and outside the ornithological reserve. Bird calls detected by BirdNET are geolocated using Flight Controller logs, and gathered into three representative groups of species. (b) Mission overview in the round pond, U.K., where the ΔT across the water–air interface is recorded and geotagged using the on-board GNSS data.**

TABLE 1. **Energetic evaluation of the different locomotion modes of SailMAV. Data is taken from field trials for all modes except for flight, which is taken from CFD simulations. Power density is calculated using the output mechanical power, while COT is calculated using the input electrical power consumed.**

Locomotion mode	Sailing	Displacement	Planing	Cruise flight
Source	field trials	field trials	field trials	CFD and thrust tests
Power density [W/kg]	-	0.1 to 5	6 to 28	3
COT [-]	0.5 to 1.4	2.8 to 4.0	4.3 to 9.8	0.8

VIII. DISCUSSION

This article presents a wide array of tests and CFD analysis, which bring insights into the performance of the vehicle and its multiple modes of locomotion: besides propelled flight in air and sailing at the water surface, Sailing-MAVs can move at the water surface using their propulsion units. While this is normally used exclusively for takeoff, it can also be used to travel in conditions of low wind, either in the slow dragging regime, or fast planing conditions—though at a severe efficiency penalty. A useful metric to evaluate these different locomotion modes is the cost of transport (COT), which is a nondimensional measurement of the amount of energy necessary for a robot to move a certain distance, given by $\text{COT} = P/(m * g * u)$.

Table 1 gives the power density and values measured experimentally for each locomotion mode performed by SailMAV. While displacement, planing and flight consider the power usage of the propellers; in sailing, only the avionics consume power. It is shown that depending on the sailing speed, flight could in some cases be a more efficient mode of transportation. A review of commercial MAVs of a similar weight class as SailMAV shows that typical COT values for MAVs carrying no payload are in the range of 0.5–0.8, so the demonstrated sailing trials can still outperform single-mode flying vehicles. Details on the platforms used for this comparison, and how the COT values were obtained are included in Supplementary Table 3.

While these previous results make it clear that sailing is a considerably more efficient form of locomotion than the other propelled locomotion alternatives at the water surface, the comparison between sailing and flight is not as straightforward. Depending on the wind speed and direction, sailing or flight could be the most efficient mode of locomotion. As shown in Fig. 14, sailing outperforms

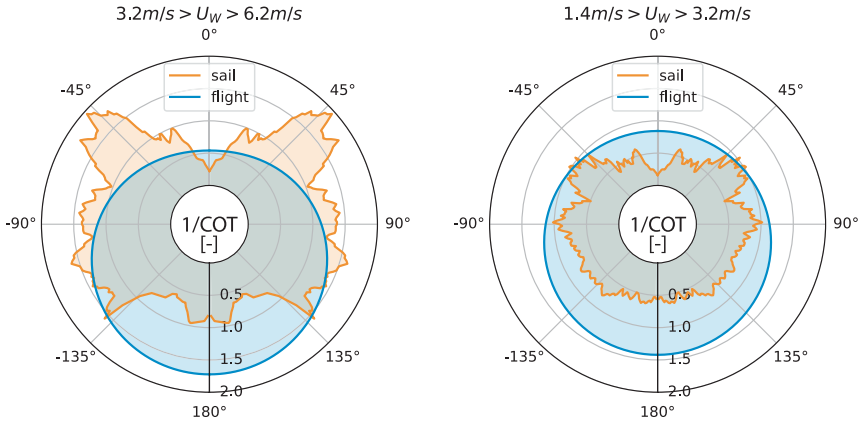

FIGURE 14. Inverse COT plotted against true wind directions, for sailing and flight modes. Sailing COT is based on field experiments, while flight COT is based on experimental and simulation data from [47].

flight at greater wind speeds, but only in the beam reaching and tacking range. In the downwind range, however, we observe sailing performance to decrease, likely due to the effect shown in Fig. 11(c). Conversely, flight consistently outperforms sailing at wind speeds lower than 3.2 m/s as the avionics power usage does not reduce at lower sailing speeds. We observed, however, that during sailing, the largest power use (80%) corresponds to the communication equipment (radio telemetry). If its transmission power was to be dynamically changed depending on the mission stages, sailing efficiency could be further improved. Finally, the fact that landing and takeoff also has a large energetic cost, it further increases the complexity of creating path planning tool which manages this type of bimodal locomotion. The collection or simulation of locomotion data for all these stages can contribute toward a decision-making tool for bimodal locomotion, a major step toward autonomous aerial–aquatic missions.

Concerning the application of SailMAV for PAM, several advantages were found for its use. Namely, unlike classic freshwater sampling methodologies which can be invasive [7], [22], [30] (with even PAM requiring bankside access, installation of buoys, or use of boats [7]), SailMAV's ability to land on and takeoff from the water surface and autonomously move across the water surface allowed us to overcome many of these challenges, requiring only limited bankside access. In fact, SailMAV was able to sail close to and even through flocks of birds with very little effect on their behavior (this is shown in Supplementary Video 10), improving the welfare standards of sampling and reducing any potential bias in data collection. The only changes in behavior we observed were individual birds moving out of the path of the robot. The spatial and temporal scale of sampling with moving and stationary approaches is considerably different. Stationary surveys allow for one area to be surveyed continuously for an extended period of days or weeks, providing repeatability. It also facilitates recording over a full 24-h period, something which was shown to be important in revealing differences in acoustic activity between habitats [19]. Moving surveys, while increasing spatial scale and coverage, do not allow for the same temporal scale, potentially obscuring differences between variables and compromising repeatability. For this reason, we believe that for many applications these methods are complementary, or the choice of method will depend on the question at hand.

IX. CONCLUSION

Small-scale water-surface robots with added flight capabilities would allow for efficient long-duration environmental data collection. However, the development of such robots is challenging due to the many concurring requirements. This article presents a framework for the design of SailMAV, supported by in-depth analysis of the different water-surface locomotion modes. Extensive fluid-dynamic modeling provided insight into the complex behavior of small-scale sailing vehicles, allowing for performance and efficiency evaluation, as well as deriving design recommendations. The developed models were also used to devise new control strategies that take advantage of rigid sails, and to design hull geometries appropriate for sailing and takeoff. A prototype was constructed and extensive field tests were conducted to showcase the developed control and navigation strategies, based on a custom sensor suite for sailing at small scales. Acoustic and environmental data is collected during long-duration outdoor missions, to demonstrate autonomous long-duration missions, and possible applications of SailMAVs.

Thanks to the insight provided, as well as the new modeling and control methods developed, this study is an essential starting point for further research on sailing–flying robots. Our extensive field tests show that the studied robotic sensing approach is highly energy-efficient, quiet, nonpolluting, and robust. The approach is therefore ideal for data collection in natural surroundings, and can provide valuable support for future research in the environmental sciences.

DATA AVAILABILITY

Supporting information is available alongside this document. Supplementary sections can be found in the file *Supplementary_sections.pdf*. Video sources referenced throughout the document and the code used for data processing can also be found in the *Supplementary_Videos* folder. The PX4 branch used for this work can be found in the Supplementary Material and in the following repository, as well as the microcontroller DAQ (repository). The 3-D models of the prototype here described as well as PCB manufacturing files are also included in Supplementary Material and available for visualization at link. Alternatively, all data and additional flight logs from field experiments, as well as corresponding postprocessing scripts can be found on Zenodo.

Acknowledgment

(ANDRÉ FARINHA and LUCA ROMANELLO contributed equally to this work.) André Farinha and Jenna Lawson were with the Aerial Robotics Laboratory, Imperial College London, London SW7 2AZ, U.K. Sophie Franziska Armanini was with eAviation Group, TUM, 80333 Munich, Germany.

REFERENCES

[1] J. C. Alves and N. A. Cruz, "FASt—An autonomous sailing platform for oceanographic missions," in *Proc. OCEANS*, Sep. 2008, pp. 1–7.

[2] H. Alzu'bi, I. Mansour, and O. Rawashdeh, "Loon copter: Implementation of a hybrid unmanned aquatic–aerial quadcopter with active buoyancy control," *J. Field Robot.*, vol. 35, no. 5, pp. 764–778, Aug. 2018.

[3] J. Cabrera-Gámez, A. Ramos de Miguel, A. C. Domínguez-Brito, J. D. Hernández-Sosa, J. Isern-González, and E. Fernández-Perdomo, "An embedded low-power control system for autonomous sailboats," in *Robotic Sailing*. Berlin, Germany: Springer, 2014, pp. 67–79.

[4] N. A. Cruz and A. C. Matos, "The MARES AUV, a modular autonomous robot for environment sampling," in *Proc. OCEANS*, Sep. 2008, pp. 1–6.

[5] I. Dathe and M. Deleo, "Hydrodynamic characteristics of seaplanes as affected by hull shape parameters," in *Proc. Adv. Mar. Vehicles Conf.*, Jun. 1989, p. 1540.

[6] S. Day et al., "ITTC recommended guidelines: Wave energy converter model test experiments (7.5–02–07–03.7)," in *Proc. 27th Int. Towing Tank Conf.*, Jan. 2014, pp. 1–13.

[7] C. Desjonquères, T. Gifford, and S. Linke, "Passive acoustic monitoring as a potential tool to survey animal and ecosystem processes in freshwater environments," *Freshwater Biol.*, vol. 65, no. 1, pp. 7–19, Jan. 2020.

[8] M. Drela, "XFOIL: An analysis and design system for low Reynolds number airfoils," in *Low Reynolds Number Aerodynamics*. Berlin, Germany: Springer, 1989, pp. 1–12.

[9] G. H. Elkaim and C. L. Boyce Jr., "Experimental aerodynamic performance of a self-trimming wing-sail for autonomous surface vehicles," *IFAC Proc. Volumes*, vol. 40, no. 17, pp. 271–276, 2007.

[10] A. Farinha, J. Di Tria, R. Zufferey, S. F. Armanini, and M. Kovac, "Challenges in control and autonomy of unmanned aerial-aquatic vehicles," in *Proc. 29th Medit. Conf. Control Autom. (MED)*, Jun. 2021, pp. 937–942.

[11] A. T. Farinha et al., "Off-shore and underwater sampling of aquatic environments with the aerial-aquatic drone Medusa," *Frontiers Environ. Sci.*, vol. 10, p. 2305, Nov. 2022.

[12] R. Gibb, E. Browning, P. Glover-Kapfer, and K. E. Jones, "Emerging opportunities and challenges for passive acoustics in ecological assessment and monitoring," *Methods Ecol. Evol.*, vol. 10, no. 2, pp. 169–185, Feb. 2019, doi: 10.1111/2041-210x.13101.

[13] L. Giger et al., "Design and construction of the autonomous sailing vessel avalon," in *Proc. World Robotic Sailing Championship Int. Robotic Sailing Conf.*, 2009, pp. 1–7, doi: 10.3929/ETHZ-A-010035784. [Online]. Available: http://hdl.handle.net/20.500.11850/82243

[14] S. Gudmundsson, *General Aviation Aircraft Design: Applied Methods and Procedures—Appendix C3 Design of Seaplanes*. Amsterdam, The Netherlands: Elsevier, Sep. 2013.

[15] L. Jaulin and F. Le Bars, "A simple controller for line following of sailboats," in *Proc. 5th Int. Robotic Sailing Conf.* Springer, 2012, pp. 117–129, doi: 10.1007/978-3-642-33084-1_11.

[16] S. Kahl, C. M. Wood, M. Eibl, and H. Klinck, "BirdNET: A deep learning solution for avian diversity monitoring," *Ecological Informat.*, vol. 61, Mar. 2021, Art. no. 101236.

[17] R. K. Katzschmann, J. DelPreto, R. MacCurdy, and D. Rus, "Exploration of underwater life with an acoustically controlled soft robotic fish," *Sci. Robot.*, vol. 3, no. 16, Mar. 2018, Art. no. eaar3449.

[18] T. L. Lam, H. Qian, Z. Wang, H. Chen, Y. Li, and Y. Xu, "System design and control of a sail-based autonomous surface vehicle," in *Proc. IEEE Int. Conf. Robot. Biomimetics (ROBIO)*, Dec. 2016, pp. 1034–1039, doi: 10.1109/ROBIO.2016.7866461.

[19] J. Lawson, A. Whitworth, and C. Banks-Leite, "Soundscapes show disruption across the diel cycle in human modified tropical landscapes," *Ecological Indicators*, vol. 144, Nov. 2022, Art. no. 109413.

[20] S. Lemaire et al., "Adaptive probabilistic tack manoeuvre decision for sailing vessels," 2019, *arXiv:1903.06677*.

[21] L. Li et al., "Aerial-aquatic robots capable of crossing the air-water boundary and hitchhiking on surfaces," *Sci. Robot.*, vol. 7, no. 66, May 2022, Art. no. eabm6695.

[22] S. Linke et al., "Freshwater ecoacoustics as a tool for continuous ecosystem monitoring," *Frontiers Ecology Environ.*, vol. 16, no. 4, pp. 231–238, May 2018.

[23] C. Lyu et al., "Toward a gliding hybrid aerial underwater vehicle: Design, fabrication, and experiments," *J. Field Robot.*, vol. 39, no. 5, pp. 543–556, Aug. 2022.

[24] L. Meier, D. Honegger, and M. Pollefeys, "PX4: A node-based multithreaded open source robotics framework for deeply embedded platforms," in *Proc. IEEE Int. Conf. Robot. Autom. (ICRA)*, May 2015, pp. 6235–6240.

[25] A. Morrall, "1957 ITTC model ship correlation line values of frictional resistance coefficient," Nat. Phys. Lab., NPL, Ship Division, Teddington, U.K., Tech. Rep., 142, 1970.

[26] F. Noblesse, "A slender-ship theory of wave resistance," *J. Ship Res.*, vol. 27, no. 1, pp. 13–33, Mar. 1983.

[27] K. Nomoto and H. Tatano, "Balance of helm of sailing yachts—A ship hydrodynamics approach on the problem," in *Proc. 6th Symp. Develop. Interest Yacht Archit.*, Amsterdam, The Netherlands, 1979, pp. 64–89.

[28] F. Plumet, C. Petrès, M.-A. Romero-Ramirez, B. Gas, and S.-H. Ieng, "Toward an autonomous sailing boat," *IEEE J. Ocean. Eng.*, vol. 40, no. 2, pp. 397–407, Apr. 2015.

[29] F. Pomati, J. Jokela, M. Simona, M. Veronesi, and B. W. Ibelings, "An automated platform for phytoplankton ecology and aquatic ecosystem monitoring," *Environ. Sci. Technol.*, vol. 45, no. 22, pp. 9658–9665, Nov. 2011.

[30] J. Radinger et al., "Effective monitoring of freshwater fish," *Fish Fisheries*, vol. 20, no. 4, pp. 729–747, Jul. 2019.

[31] F. Rockenbauer et al., "Dipper: A dynamically transitioning aerial-aquatic unmanned vehicle," in *Proc. Robot., Sci. Syst.*, Jul. 2021, pp. 12–16.

[32] P. F. Rynne and K. D. von Ellenrieder, "Unmanned autonomous sailing: Current status and future role in sustained ocean observations," *Mar. Technol. Soc. J.*, vol. 43, no. 1, pp. 21–30, Mar. 2009.

[33] Saildrone. (2019). *Antarctica Circumnavigation 2019 Surface and Adcp Measurements*. [Online]. Available: https://data.saildrone.com/id/2091

[34] K. Ragib Ishraq Sanim et al., "Development of an aerial drone system for water analysis and sampling," in *Proc. Int. Conf. Unmanned Aircr. Syst. (ICUAS)*, Jun. 2022, pp. 1601–1607.

[35] D. Savitsky, "Hydrodynamic design of planing hulls," *Mar. Technol. SNAME News*, vol. 1, no. 4, pp. 71–95, Oct. 1964.

[36] R. Siddall and M. Kovač, "Launching the AquaMAV: Bioinspired design for aerial–aquatic robotic platforms," *Bioinspiration Biomimetics*, vol. 9, no. 3, Mar. 2014, Art. no. 031001, doi: 10.1088/1748-3182/9/3/031001.

[37] C. Son, P. K. Sahoo, V. Aribenchi, and S. Asapana, "CFD simulation of resistance of highspeed trimaran hullforms," in *Proc. 13th Int. Conf. Fast Sea Transp.*, 2015, Paper SNAME-FAST-2015-011. [Online]. Available: https://doi.org/10.5957/FAST-2015-011

[38] R. Stelzer and K. Jafarmadar, "History and recent developments in robotic sailing," in *Proc. 4th Int. Robotic Sailing Conf.* Springer, 2011, pp. 3–23.

[39] R. Stelzer and T. Pröll, "Autonomous sailboat navigation for short course racing," *Robot. Auto. Syst.*, vol. 56, no. 7, pp. 604–614, Jul. 2008, doi: 10.1016/j.robot.2007.10.004. [Online]. Available: https://www.sciencedirect.com/science/article/pii/S0921889007001480

[40] W. Stewart et al., "Design and demonstration of a seabird-inspired fixed-wing hybrid UAV-UUV system," *Bioinspiration Biomimetics*, vol. 13, no. 5, Aug. 2018, Art. no. 056013.

[41] L. S. M. Sugai, T. S. F. Silva, J. W. Ribeiro, and D. Llusia, "Terrestrial passive acoustic monitoring: Review and perspectives," *BioScience*, vol. 69, no. 1, pp. 15–25, Jan. 2019.

[42] Q. Sun, W. Qi, H. Liu, X. Ji, and H. Qian, "Toward long-term sailing robots: State of the art from energy perspectives," *Frontiers Robot. AI*, vol. 8, Jan. 2022, Art. no. 787253, doi: 10.3389/frobt.2021.787253.

[43] C. Viel, U. Vautier, J. Wan, and L. Jaulin, "Position keeping control of an autonomous sailboat," *IFAC-PapersOnLine*, vol. 51, no. 29, pp. 14–19, 2018.

[44] Z. Wei, Y. Teng, X. Meng, B. Yao, and L. Lian, "Lifting-principle-based design and implementation of fixed-wing unmanned aerial–underwater vehicle," *J. Field Robot.*, vol. 39, no. 6, pp. 694–711, Sep. 2022.

[45] R. R. Wilson, D. J. Twedt, and A. B. Elliott, "Comparison of line transects and point counts for monitoring spring migration in forested wetlands," *J. Field Ornithol.*, vol. 71, no. 2, pp. 345–355, Jun. 2000.

[46] Z. Zeng, C. Lyu, Y. Bi, Y. Jin, D. Lu, and L. Lian, "Review of hybrid aerial underwater vehicle: Cross-domain mobility and transitions control," *Ocean Eng.*, vol. 248, Mar. 2022, Art. no. 110840.

[47] R. Zufferey et al., "SailMAV: Design and implementation of a novel multi-modal flying sailing robot," *IEEE Robot. Autom. Lett.*, vol. 4, no. 3, pp. 2894–2901, Jul. 2019.

[48] R. Zufferey, S. F. Armanini, A. Farinha, and M. Kovač, "Adaptive morphology in aerial-aquatic robots," in *Proc. 9th Int. Symp. Adapt. Motion Animals Mach. (AMAM)*, Jan. 2019, Paperamam2019-151038, doi: 10.5075/epfl-biorob-amam2019-38.

[49] R. Zufferey, R. Siddall, S. F. Armanini, and M. Kovac, *Between Sea and Sky: Aerial Aquatic Locomotion in Miniature Robots*. Berlin, Germany: Springer, 2022.